

# Convection-Permitting Simulations with the E3SM Global Atmosphere Model

P. M. Caldwell<sup>1</sup>, C. R. Terai<sup>1</sup>, B. Hillman<sup>2</sup>, N. D. Keen<sup>3</sup>, P. Bogenschutz<sup>1</sup>, W. Lin<sup>4</sup>, H. Beydoun<sup>1</sup>, M. Taylor<sup>2</sup>, L. Bertagna<sup>2</sup>, A. M. Bradley<sup>2</sup>, T. C. Clevenger<sup>2</sup>, A. S. Donahue<sup>1</sup>, C. Eldred<sup>2</sup>, J. Foucar<sup>2</sup>, J.-C. Golaz<sup>1</sup>, O. Guba<sup>2</sup>, R. Jacob<sup>5</sup>, J. Johnson<sup>6</sup>, J. Krishna<sup>5</sup>, W. Liu<sup>7</sup>, K. Pressel<sup>8</sup>, A. G. Salinger<sup>2</sup>, B. Singh<sup>8</sup>, A. Steyer<sup>2</sup>, P. Ullrich<sup>7</sup>, D. Wu<sup>5</sup>, X. Yuan<sup>5</sup>, J. Shpund<sup>8</sup>, H.-Y. Ma<sup>1</sup>, C. S. Zender<sup>9</sup>

<sup>1</sup>Lawrence Livermore National Lab, Livermore, CA, USA

<sup>2</sup>Sandia National Lab, Albuquerque, NM, USA

<sup>3</sup>Lawrence Berkeley National Lab, Berkeley, CA, USA

<sup>4</sup>Brookhaven National Lab, Upton, NY, USA

<sup>5</sup>Argonne National Lab, Lemont, IL, USA

<sup>6</sup>Cohere Consulting LLC, Seattle, WA, USA

<sup>7</sup>Department of Land, Air, and Water Resources, University of California-Davis, Davis, CA, USA

<sup>8</sup>Pacific Northwest National Lab, Richland, WA, USA

<sup>9</sup>Departments of Earth System Science and Computer Science, University of California, Irvine, USA

## Key Points:

- Describes the Simple Cloud-Resolving E3SM Atmosphere Model (SCREAM)
- SCREAM performs well in a 40 day boreal winter simulation at 3.25 km  $\Delta x$
- Resolving deep convection solves many long-standing climate model biases

---

Corresponding author: Peter Caldwell, [caldwell119@llnl.gov](mailto:caldwell119@llnl.gov)

**Abstract**

This paper describes the first implementation of the  $\Delta x = 3.25$  km version of the Energy Exascale Earth System Model (E3SM) global atmosphere model and its behavior in a 40 day prescribed-sea-surface-temperature simulation (Jan 20 through Feb 28, 2020). This simulation was performed as part of the DYnamics of the Atmospheric general circulation Modeled On Non-hydrostatic Domains (DYAMOND) phase 2 model intercomparison. Effective resolution is found to be  $\sim 6\times$  the horizontal dynamics grid resolution despite using a coarser grid for physical parameterizations. Despite this new model being in an immature and untuned state, moving to 3.25 km grid spacing solves several long-standing problems with the E3SM model. In particular, Amazon precipitation is much more realistic, the frequency of light and heavy precipitation is improved, agreement between the simulated and observed diurnal cycle of tropical precipitation is excellent, and the vertical structure of tropical convection and coastal stratocumulus look good. In addition, the new model is able to capture the frequency and structure of important weather events (e.g. tropical cyclones, extratropical cyclones including atmospheric rivers, and cold air outbreaks). Interestingly, this model does *not* get rid of the erroneous southern branch of the intertropical convergence zone nor the tendency for strongest convection to occur over the Maritime Continent rather than the West Pacific, both of which are classic climate model biases. Several other problems with the simulation are identified, underscoring the fact that this model is a work in progress.

**Plain Language Summary**

This paper describes the new global 3.25 km version of the Energy Exascale Earth System Model (E3SM) atmosphere model and its behavior in a 40-day northern-hemisphere wintertime simulation. In exchange for huge computational expense, this high-resolution model avoids many but not all biases common in lower-resolution models. It also captures several types of extreme weather that would simply not be resolved in lower-resolution models. Several opportunities for further development are identified.

**1 Introduction**

Because the processes controlling Earth's weather and its climatology are complex and inter-related, numerical models are a critical tool for predicting future conditions. Global coverage is necessary because local behavior propagates rapidly to distant areas of the globe. Simulating the whole planet imposes severe computational challenges, however. In the past, this has typically been handled by coarsening model grid spacing until simulations became affordable on the machines of the time. As of 2020, this translated to horizontal grid spacing of  $\sim 10$  km for weather models (which simulate days to weeks at a time) and  $\sim 100$  km for climate models (which are typically run for centuries). These grid spacings are too coarse to capture many important atmospheric processes.

The impacts of sub-grid scale processes on model climate are instead *parameterized* based on available grid-scale quantities. Typical parameterized processes include turbulent transport and mixing, gravity-wave motions, greenhouse gas and aerosol chemistry and physics, radiative transfer, and cloud physics. Cloud parameterizations are in particular complicated yet important for accurate predictions. Vapor transport, collisions, and other physics involving micron-scale water drops or ice crystals (collectively called microphysics) are critical for predicting precipitation and future changes in cloud shading. Condensation and evaporation of clouds and resulting fractional cloudiness within a grid cell (often called macrophysics) involve larger spatial scales but are still important to parameterize in conventional models. Condensational heating in convective clouds causes narrow but intense upward vertical motions which are a primary source of vertical transport of heat, moisture, and momentum in the tropical atmosphere (Riehl & Malkus, 1958). Because the microphysics and macrophysics of these intense updrafts are

72 tightly entwined with their motions, convective parameterizations tend to include their  
73 own microphysics and macrophysics treatments. Inconsistency between microphysical  
74 treatments for convective- versus resolved-scale motions is a large source of model bi-  
75 ases (Song & Zhang, 2011; Storer et al., 2015). Convection in general has proven to be  
76 particularly difficult to parameterize from quantities available on the grid scale (Randall  
77 et al., 2003; Stevens & Bony, 2013) and has been implicated as a primary source of cli-  
78 mate change uncertainty (Sanderson et al., 2008; Sherwood et al., 2014).

79 Another challenge posed by coarse resolution is interaction with Earth’s surface.  
80 Topography is not resolved at typical global model grid spacing and in fact must be even  
81 further smoothed to avoid model instability (Lauritzen et al., 2015). Because topogra-  
82 phy can force air upwards until it condenses, smoothing out high mountain peaks causes  
83 major problems for cloud and precipitation climatology (Giorgi & Marinucci, 1996). In-  
84 sufficient surface roughness means wind stresses are also too weak over smoothed topog-  
85 raphy and must be parameterized. Subgrid-scale surface heterogeneity also poses prob-  
86 lems for coarse models (Prein et al., 2015). And while the focus of this paper is on sim-  
87 ulations with prescribed sea surface temperature, it is worth noting that ocean eddies  
88 on spatial scales  $<10$  km play a critical role in heat transport (Maslowski et al., 2008)  
89 and their parameterization has proven as problematic for ocean models as convective clouds  
90 are for atmosphere models (Hewitt et al., 2020). Ocean/atmosphere interaction at convection-  
91 and ocean-eddy resolving scales has not (to our knowledge) been studied but is also likely  
92 to have important impacts on model behavior.

93 Because so much is lost at coarse resolution, the global atmospheric modeling com-  
94 munity has long pushed towards higher resolution. Unsurprisingly, better topographic  
95 resolution improves orographic precipitation, snowpack, and stream flow (Pope & Strat-  
96 ton, 2002; Duffy et al., 2003; Delworth et al., 2012; Caldwell et al., 2019). Sea breeze ef-  
97 fects become better captured as coastal boundaries are better resolved (Boyle & Klein,  
98 2010; Love et al., 2011). Because finer grid spacing allows smaller spatial and temporal  
99 scales to be resolved, higher-resolution GCMs also better capture extreme precipitation  
100 events (Iorio et al., 2004; Wehner et al., 2014; Terai et al., 2018). As GCM grid spac-  
101 ing falls to 25 km or less, tropical cyclones begin to be resolved (Atlas et al., 2005; Bacmeis-  
102 ter et al., 2014; Wehner et al., 2014; Caldwell et al., 2019), though capturing details of  
103 spatial structure requires still finer resolution (Judt et al., 2021). Some classic model prob-  
104 lems are, however, relatively unaffected by reducing grid spacing to 25 km. In partic-  
105 ular, increased resolution does not get rid of the erroneous southern branch of the In-  
106 tertropical Convergence Zone (ITCZ) common in climate models (McClellan et al., 2011;  
107 Bacmeister et al., 2014; Caldwell et al., 2019). Simulation of the Madden-Julian Oscil-  
108 lation (MJO) is likewise unaffected (Jung et al., 2012; Bacmeister et al., 2014). In ad-  
109 dition, precipitation improvement has been found primarily in wintertime (Duffy et al.,  
110 2003).

111 It is notable that these remaining deficiencies are related to convective motions which  
112 are unresolved even at high GCM resolutions. Given the aforementioned difficulty of pa-  
113 rameterizing convection, this situation is perhaps expected. A small number of global  
114 models with grid spacing fine enough to explicitly resolve the largest convection events  
115 (hereafter called global convection-permitting models or GCPMs) have also been built.  
116 The number of these models has exploded recently because recent advances in comput-  
117 ing have tended towards allowing more calculations to be performed in parallel rather  
118 than making individual calculations faster. Conventional global simulations already ex-  
119 ploit all available parallelism, so won’t run faster on these new machines. Higher hor-  
120 izontal resolution is a ready source of increased parallelism, so is attractive in this new  
121 computing environment. Unfortunately, smaller timesteps are needed to resolve finer spa-  
122 tial scales. Thus even if all columns could be computed in parallel, a given integration  
123 at finer resolution requires more timesteps and therefore has a longer time-to-solution.

124 As a result, GCPM simulations can't be run as routinely nor as long as conventional global  
125 models.

126 The history of GCPM modeling is nicely summarized in Satoh et al. (2019). Briefly,  
127 the first GCPM was NICAM, described in Tomita et al. (2005); Satoh et al. (2008, 2014).  
128 For several years its only companion was the Multiscale Modeling Framework (MMF)  
129 described in Grabowski and Smolarkiewicz (1999), Randall et al. (2003), and Grabowski  
130 (2016). The MMF isn't exactly a GCPM, however, as it replaces the physical param-  
131 eterizations inside each grid cell of a conventional GCM with a limited-area convection-  
132 permitting model (CPM). The MMF is much cheaper than a GCPM because embedded  
133 CPMs are typically contained within a single computational node, avoiding MPI com-  
134 munication costs. Additionally, the grid of the CPM is decoupled from that of the GCM,  
135 so CPMs are typically 2d and have domain size smaller than the GCM grid cell width.  
136 The second GCPM was NASA's GEOS model (Putman & Suarez, 2011), which was used  
137 as a synthetic laboratory for designing and testing satellite campaigns (Gelaro et al., 2015)  
138 in addition to more general analysis. In the last few years, enough new GCPMs have been  
139 developed to warrant their own intercomparison. Called DYnamics of the Atmospheric  
140 general circulation Modeled On Nonhydrostatic Domains (DYAMOND), the first phase  
141 of this intercomparison focused on a 40 day simulation starting Aug 1, 2016 and included  
142 8 models with grid spacing less than 5 km globally. An overview of this intercompari-  
143 son is presented in Stevens et al. (2019). Stevens' study shows striking agreement in out-  
144 going longwave radiation, precipitation, and precipitable water between participating mod-  
145 els. Shortwave radiation differs between models, presumably due to differences in low  
146 clouds, which aren't well resolved at GCPM resolutions. Models also tend to predict a  
147 spurious peak in precipitation just south of the equator, suggesting that km-scale res-  
148 olution is not the solution to the double-ITCZ problem endemic to conventional climate  
149 models (Li & Xie, 2014). Based on the success of this first intercomparison, a second DYA-  
150 MOND intercomparison (called DYAMOND2) is now underway. The current paper docu-  
151 ments a new contribution to DYAMOND2.

152 GCPMs can be viewed as a natural and beneficial extension of conventional GCMs  
153 to finer resolution, but they can also be seen as the extension towards larger domains  
154 of a robust research community focused on limited-area CPMs. Beginning with the ex-  
155 plicit simulation of a single convective event (Ogura, 1963), cloud-resolving simulations  
156 have steadily grown in duration and domain size. Recently, Bretherton and Khairout-  
157 dinov (2015) and Narenpitak et al. (2017) describe multi-month 4 km simulations sim-  
158 ulating the entire tropical channel between 45°N and 45°S. CPMs tend to offer more ben-  
159 efit for summertime convection rather than wintertime cyclones (Prein et al., 2015), as  
160 may be expected given the spatial scale of these storm types. Limited-area CPM research  
161 suggests that resolution finer than ~4 km is needed to resolve convective ensemble statis-  
162 tics (Weisman et al. (1997); also found for GCPMs by Miyamoto et al. (2013)) but res-  
163 olution finer than that adds relatively little value (Kain et al., 2008; Schwartz et al., 2009;  
164 Langhans et al., 2013). Cloud fraction tends to decrease as resolution becomes finer (Prein  
165 et al., 2013; Langhans et al., 2013; Fosser et al., 2014), a feature also found in GCPMs  
166 (Noda et al., 2010; Hohenegger et al., 2020).

167 A great deal of CPM research has been organized around the Global Energy and  
168 Water Cycle Experiment Cloud Systems Study (GCSS). As described in a review by Krueger  
169 et al. (2016), GCSS organized intercomparisons of CPMs and single-column versions of  
170 GCMs for intensive observing periods spanning a wide variety of cloud regimes. These  
171 intercomparisons clarified processes CPMs could and couldn't handle, often leading to  
172 idealized follow-up experiments. These follow-up studies have proven invaluable for pro-  
173 viding process insights and subsequent model improvements. DYAMOND is in some ways  
174 the reincarnation of GCSS for the next generation of models.

175 In general, high-resolution regional studies have added value primarily by resolv-  
176 ing fine-scale features rather than through upscale effects onto scales resolved by con-

177 ventional models (Prein et al., 2015; Caldwell, 2010). One potential reason for this is that  
 178 lateral boundary conditions impose strong constraints on domain-averaged properties  
 179 (Edman & Romps, 2014). Thus while GCPMs may be overkill for looking at fine-scale  
 180 features which could be studied via limited-area models, they offer fresh new potential  
 181 to solve long-standing deficiencies in the general circulation.

182 The goal of this paper is to introduce the GCPM being developed by the Energy  
 183 Exascale Earth System Model (E3SM) project and to provide an initial look at its be-  
 184 havior in the DYAMOND2 case study. Details about this model are provided in Section 2.  
 185 Sections 3-5 describe experimental design, data for evaluation, and computational per-  
 186 formance (respectively). Results in Section 6 are broken into an analysis of effective res-  
 187 olution in subsection 6.1, general attributes in subsection 6.2, clouds and radiation in  
 188 subsection 6.3, precipitation in subsection 6.4, and specific weather phenomena in sub-  
 189 sequent subsections. Conclusions follow in Section 7.

## 190 2 Model Description

191 As described in Golaz et al. (2019), the E3SM project was born from the US De-  
 192 partment of Energy (DOE)’s need for quantitative information about future climate for  
 193 use in energy-sector decisions. Given DOE’s leadership in high-performance computing,  
 194 it has been natural for E3SM to focus on compute-intensive frontiers in climate science.  
 195 One of those efforts has been to develop a new GCPM called the Simple Cloud-Resolving  
 196 E3SM Atmosphere Model (SCREAM).

197 Our ultimate goal is to make SCREAM as fast as possible on exascale machines  
 198 by writing it in C++ using the Kokkos library (Carter-Edwards et al., 2014) for perfor-  
 199 mance portability. See Bertagna et al. (2019, 2020) for a description of our design strat-  
 200 egy and initial performance results. We are, however, approaching this goal by first cre-  
 201 ating a prototype version in Fortran using the existing E3SM atmosphere infrastructure.  
 202 This initial implementation - which is the focus of the current study - is being used as  
 203 the template for the C++ implementation as well as giving us an early look at model  
 204 behavior. The final implementation should be scientifically identical to this prototype  
 205 version but will be much faster because of its ability to run on GPU-powered comput-  
 206 ers.

207 Our strategy has been to make our first implementation as simple as possible and  
 208 to start using it for science as quickly as possible. This strategy is expected to result in  
 209 sub-optimal skill in our first implementation, but allows us to more rapidly produce, un-  
 210 derstand, and improve our model. We believe that it is better to start with an overly-  
 211 simple model and to add complexity as needed rather than to start with a more sophis-  
 212 ticated/accurate model which we don’t understand.

213 Simplicity in particular means that SCREAM consists solely of nonhydrostatic fluid  
 214 dynamics, a turbulence/cloud fraction scheme, a microphysics scheme, a radiation scheme,  
 215 an energy fixer, and prescribed-aerosol functionality. These pieces are described in the  
 216 subsections below. SCREAM does not parameterize sub-grid scale gravity-wave drag or  
 217 deep convection. This initial implementation uses the E3SM land model described in Golaz  
 218 et al. (2019). It also uses prescribed-ice mode from CICE4 (Hunke & Lipscomb, 2008)  
 219 to compute surface fluxes, snow depth, albedos, and surface temperature, resetting sea  
 220 ice thickness after each timestep to 2 m in the northern hemisphere and 1 m in the south-  
 221 ern hemisphere. Sea surface temperature (SST) is prescribed.

### 222 2.1 Fluid Dynamics

223 SCREAM’s fluid-dynamics solver (hereafter dycore) solves the nonhydrostatic equa-  
 224 tions of motion in a rotating reference frame with the shallow atmosphere approxima-

tion and a hyperviscosity based turbulence closure. It additionally transports several constituents, including multiple forms of water and various aerosols. It is implemented in the High Order Method Modeling Environment (HOMME) (Dennis et al., 2005, 2012; Evans et al., 2013). HOMME contains several spectral element based dycores, including the hydrostatic dycore used by E3SM (Rasch et al., 2019; Golaz et al., 2019; Caldwell et al., 2019) and the Community Earth System Model (Small et al., 2014; S. Zhang et al., 2020). We refer to the new nonhydrostatic dycore developed for SCREAM as HOMME-NH.

HOMME-NH uses the nonhydrostatic formulation of the equations from Taylor et al. (2020). It solves the equations in a terrain following mass based vertical coordinate (Kasahara, 1974; Laprise, 1992), with prognostic equations for the three components of the velocity field, the mass-coordinate pseudo-density, the geopotential height, and a thermodynamic variable, for which we use virtual potential temperature. The prognostic equations consist of the time-reversible adiabatic terms from Taylor et al. (2020), a  $\nabla^4$  hyperviscosity following Dennis et al. (2012) and Guba et al. (2014), and a sponge layer at the model top. For the adiabatic terms, we use a structure preserving formulation in order to preserve the discrete Hamiltonian and produce an energetically consistent model. The horizontal discretization uses the collocated mimetic spectral element method from Taylor and Fournier (2010), with conservative and monotone semi-Lagrangian tracer transport (Bradley et al., 2019). The vertical discretization uses a Lorenz staggered extension of the mimetic centered difference from Simmons and Burridge (1981). With this vertical staggering, prognostic variables are located at level midpoints, with the exception of the vertical velocity and geopotential, which are located at level interfaces. For the vertical transport terms, we use a vertically Lagrangian approach adapted from Lin (2004).

For the temporal discretization, we use a Horizontally Explicit Vertically Implicit (HEVI) approach (Satoh, 2002), discretized with an IMPLICIT-EXPLICIT (IMEX) Runge Kutta method (Ascher et al., 1997). The HEVI splitting decomposes the equations into a set of terms which represent vertically propagating acoustic waves (treated implicitly), and the remaining terms which include all horizontal derivatives (treated explicitly). We use a highly efficient IMEX method from Steyer et al. (2019) and Guba et al. (2020), with a 2nd-order accurate coupling of a high-stage high-CFL scheme for the explicit terms and a Diagonally Implicit Runge Kutta (DIRK) scheme for the implicit terms. Due to the use of the Laprise mass coordinate, the vertical acoustic waves are isolated to only two terms in the equations for vertical velocity and geopotential solved at level interfaces, leading to an implicit system for a single variable.

There are several sources of dissipation in the dynamical core. The  $\nabla^4$  hyperviscosity is the largest. It is applied to all prognostic variables and on every model layer, with a hyperviscosity coefficient of  $2.5 \times 10^{10} \text{ m}^4 \text{ s}^{-1}$  for the 3.25 km grid. Because tuning at 3.25 km is expensive, we chose this value based on a  $\Delta x^3$  scaling of the hyperviscosity coefficient used by E3SM at lower resolutions. For the model-top sponge-layer, we applied a  $\nabla^2$  Laplacian operator to all prognostic variables according to the reference-pressure based ramp function from Lauritzen et al. (2011). This ramp starts at layer 14 ( $\sim 19\text{hPa}$ ) with a coefficient of  $0.189 \times 10^{-4} \text{ m}^2 \text{ s}^{-1}$  and ramps up to  $6.93 \times 10^{-4} \text{ m}^2 \text{ s}^{-1}$  at the model top. In addition, vertical dissipation is introduced by the monotone vertical remap operator. A smaller amount of dissipation is also generated by the Runge-Kutta timestepping.

## 2.2 Model Grid

Our horizontal grid for dynamics is a cubed-sphere grid with  $1024 \times 1024$  spectral elements on each face, denoted ne1024. The total number of elements is therefore 6,291,456. Within each element, fields are represented by degree-3 polynomials, using nodal values

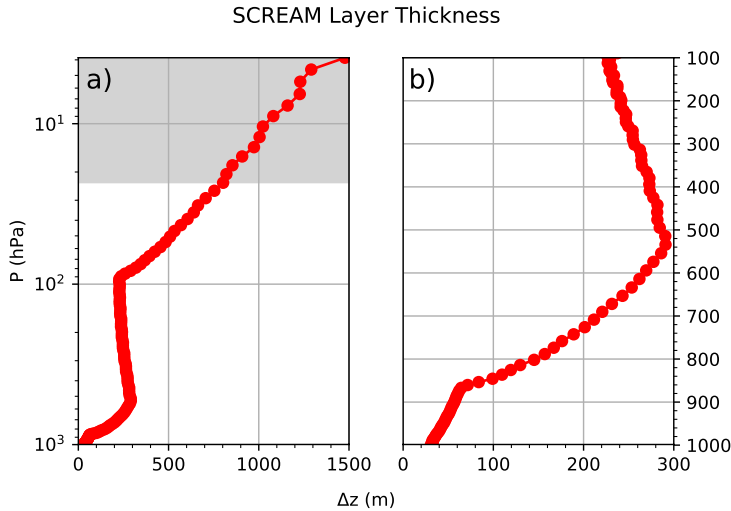


**Figure 1.** SCREAM grid spacing. Panel a shows the complete vertical grid using logarithmic pressure to emphasize the upper atmosphere. Panel b zooms in on the troposphere using linear pressure spacing to emphasize lower levels. The sponge layer is indicated by gray-shading.

276 on a  $4 \times 4$  grid of Gauss-Lobatto-Legendre (GLL) nodes. The edge and corner nodes are  
 277 shared by adjacent elements, resulting in an average spacing between GLL nodes of  $\sim 3.25$   
 278 km. The nonuniform spacing of GLL nodes presents some challenges to the physical pa-  
 279 rameterizations (Herrington et al., 2019), which we avoid by evaluating the parameter-  
 280 izations on a uniformly spaced  $2 \times 2$  grid within each spectral element. This *physics grid*  
 281 has  $4/9$  as many physics columns as would be in a GLL-located physics grid. Tests  
 282 show that the  $2 \times 2$  physics grid provides very similar results to simulations with physics  
 283 running on every GLL node (Hannah et al., 2021). Our land model is run on a  $1/8^\circ$  latitude-  
 284 longitude grid. SST and sea ice are computed on the high-resolution ocean grid used by  
 285 Caldwell et al. (2019), which tapers from 18 km in the tropics to 6 km near the poles.  
 286 The ocean and sea ice grids have minor impact since SST and ice extent are interpolated  
 287 from  $0.5^\circ$  datasets. It would be better to have all surface calculation on the 3.25 km at-  
 288 mosphere grid, but resolution challenges with the E3SM input data toolchain made doing  
 289 so impractical for this initial simulation.

290 We use a relatively-fine 128 layer vertical grid with a model top at 40 km (2.25 hPa)  
 291 and a sponge layer above  $\sim 19$  hPa (as as described in the previous subsection). Verti-  
 292 cal grid spacing is presented in Fig. 1. Representative grid spacing in the boundary layer  
 293 is  $\sim 50$  m, in trade Cu is  $\sim 100$  m, and in tropical cirrus anvils is  $\sim 250$  m.

### 294 2.3 Topography

295 To generate the SCREAM v0 surface topography, we use the NCAR topography  
 296 tool chain (Lauritzen et al., 2015) to first compute the unfiltered height field on the at-  
 297 mosphere grid. We then smooth the height field on the GLL grid using 16 iterations of  
 298 the spectral element Laplace operator. To quantify the amount of smoothing, we follow  
 299 Evans et al. (2013) and compare power spectra  $E(k)$  from the spherical harmonic rep-  
 300 resentation of the filtered and unfiltered height field, and then compute the lowest wave  
 301 number  $k_{1/2}$  for which the smoothing has reduced  $E(k_{1/2})$  by 50%. The SCREAM v0  
 302 topography has a  $k_{1/2}$  corresponding to wavelength  $6.4\Delta x$ .

## 2.4 Clouds and Turbulence

Boundary layer clouds and their associated circulations are still largely unresolved at 3.25 km so a parameterization of interaction between clouds and turbulence is critical. Because GCPMs push the boundary of computational possibility, it is important that these processes are handled efficiently. These goals are accomplished in SCREAM via the Simplified Higher Order Closure (SHOC; Bogenschutz & Krueger, 2013). Similar to other widely used assumed PDF-based schemes (Golaz et al., 2002; Cheng & Xu, 2008), SHOC computes subgrid-scale liquid cloud and turbulence using an assumed double-Gaussian probability density function (PDF). SHOC is more efficient than the aforementioned schemes, however, because it diagnoses rather than prognoses the higher order moments that are needed to close the double Gaussian PDF. Bogenschutz and Krueger (2013) demonstrate that when SHOC is used in limited-area cloud-resolving simulations of boundary layer clouds, the solution is insensitive to the horizontal resolution choice. This is in contrast to a standard 1.5-order TKE closure, which suffers from large horizontal-resolution sensitivity when used in the same cloud-resolving model.

SHOC has undergone several updates since Bogenschutz and Krueger (2013) to improve numerical stability and performance among the wider range of regimes SHOC is subjected to in a global model. Chief among these updates is the implementation of an implicit diffusion solver, a revised formulation of the turbulence length scale to better achieve vertical convergence, and a revised formulation of the eddy diffusivities for the stable boundary layer (similar to those implemented in Bretherton and Park (2009)). The turbulence length scale is now a continuous formulation that avoids the separate definitions of in-cloud vs sub-cloud length scales documented in Bogenschutz and Krueger (2013) and performs scientifically similarly to the original formulation.

In addition to the liquid cloud fraction supplied by SHOC, we require an ice cloud fraction. For simplicity, our initial implementation includes the same ice cloud fraction used by E3SMv1 and inherited from CESM1. This implementation assumes ice cloud starts forming when an ice-modified relative humidity  $RH_i = (q_v + q_i)/q_{\text{sat},i}$  reaches a user-specified minimum value and reaches 100% at a user-specified maximum value. Unfortunately, these parameters were left at their low-resolution E3SMv1 defaults of 80% and 105% (respectively) in our DYAMOND2 simulation. The impact of this mistake is shown in Section 6.2.

## 2.5 Microphysics

SCREAM microphysics is based on the Predicted Particle Properties (P3) scheme of Morrison and Milbrandt (2015) taken from version 4.1 of the Weather Research and Forecasting (WRF) model (Skamarock et al., 2019). The novel feature of P3 is that it avoids arbitrary cutoffs between cloud-borne and precipitating ice categories by employing a single ice category which is allowed to evolve naturally from small pristine crystals into large and possibly rimed snowflakes. While the WRF version of P3 allows for multiple simultaneous populations of these ice crystals within a grid cell, SCREAM currently only supports a single population because the modest improvements from multiple ice populations reported in Milbrandt and Morrison (2016) were not deemed worth the additional software engineering time required to support this feature. The liquid phase of the P3 scheme - like most microphysics codes - separates drops into cloud and rain categories.

One feature of this scheme is the clever use of supersaturation to diagnose condensation, evaporation, sublimation, and deposition. This approach works well for Large-Eddy simulations (LES) which explicitly model each updraft, but probably underpredicts condensation for the 3.25 km grid spacing used in SCREAM (Morrison & Grabowski, 2008). The great benefit of this supersaturation approach is that it treats ice growth at the expense of nearby liquid (Wegener, 1911; Bergeron, 1935; Findeisen, 1938, hereafter

354 WBF process) in a very natural way. Unfortunately, allowing supersaturation in P3 di-  
 355 rectly conflicts with the instantaneous saturation adjustment assumption which forms  
 356 the foundation of SHOC’s PDF. For consistency, our P3 implementation instead han-  
 357 dles vapor deposition, sublimation, and the associated WBF process following Gettelman  
 358 and Morrison (2015). In particular, maximum overlap between liquid and ice is assumed  
 359 when liquid and ice coexist, leading to efficient liquid-to-ice transition via the WBF pro-  
 360 cess. If all liquid is removed within a microphysics timestep, vapor deposition onto ice  
 361 for the remainder of that timestep is computed based on cell-average water vapor con-  
 362 tent.

363 Another inconsistency between SHOC and the WRF version of P3 is the use of frac-  
 364 tional cloudiness and precipitation. P3 neglected all sub-grid variability such that cloud  
 365 and precipitation covered the entire grid cell where they exist and otherwise the cell was  
 366 entirely devoid of condensate. SHOC provides fractional cloudiness, so we modified P3  
 367 to only operate in the cloudy or precipitating portion of each cell. Our fractional cloudi-  
 368 ness implementation is similar to Jouan et al. (2020), which was implemented in WRF  
 369 P3 around the same time as we made our modifications. The fraction of each cell con-  
 370 taining precipitation is also important. In SCREAM this was taken to be equal to the  
 371 largest cloud fraction of all cells including and above the layer of interest. This approach  
 372 is crude (as noted by Zheng et al., 2020) and will be a subject of future research.

373 SHOC’s subgrid assumptions require further modifications. SHOC uses a double-  
 374 Gaussian PDF to model subgrid-scale variations in liquid water potential temperature,  
 375 total water mixing ratio, and vertical velocity. Larson and Griffin (2013) provide an an-  
 376 alytical formulation for incorporating SHOC’s variability into microphysical processes  
 377 expressed as power functions. We intend to implement this consistent scheme in our ver-  
 378 sion of P3 eventually, but for the moment we have instead implemented the partially-  
 379 consistent approach from (Morrison & Gettelman, 2008), which instead assumes a gamma  
 380 distribution for liquid water mixing ratio and ignores subgrid temperature variations.  
 381 The benefit of the gamma distribution is that the expected value of a power-law-based  
 382 microphysical process rate can be written as that power law applied to the cell-mean value  
 383 multiplied by an easily-calculated scaling factor.

384 Finally, water vapor saturation was changed in our version of P3 to be consistent  
 385 with the Murphy and Koop (2005) (MK) implementation used in SHOC. MK is more  
 386 accurate at very low temperatures than the Flatau et al. (1992) implementation origi-  
 387 nally used in P3, but is more computationally expensive. We found this performance  
 388 difference, however, to have a negligible impact on total run time.

## 389 2.6 Radiation

390 Gas optical properties and radiative fluxes are computed using the RTE+RRTMGP  
 391 radiative transfer package (Pincus et al., 2019). Active gases in SCREAM include H<sub>2</sub>O,  
 392 CO<sub>2</sub>, O<sub>3</sub>, N<sub>2</sub>O, CO, CH<sub>4</sub>, O<sub>2</sub>, and N<sub>2</sub>. Cloud and aerosol optical properties are computed  
 393 as in the Community Atmosphere Model (CAM). The approach is described in detail  
 394 in Neale et al. (2012). Briefly, condensed phase optical properties (extinction coefficient,  
 395 single scattering albedo, and asymmetry parameter for shortwave bands and absorption  
 396 coefficient for longwave bands) are computed per unit mass for liquid, ice, and aerosol,  
 397 then multiplied by the appropriate mass mixing ratio for use in RTE+RRTMGP.

398 Liquid cloud optical properties are calculated from a table-lookup after being com-  
 399 puted offline using a Mie scattering code (Wiscombe, 1996) based on the assumption (taken  
 400 from microphysics) that the total number of liquid drops with diameter  $D$  follows a gamma  
 401 histogram

$$n(D) = N_0 D^\mu e^{-\lambda D}$$

with intercept parameter  $N_0$ , slope parameter  $\lambda$ , and spectral size dispersion  $\mu$  taken every timestep from P3. In this initial implementation, in-cloud liquid water content is assumed to be homogeneously distributed. This is inconsistent with our implementation of P3, which (as noted above) assumes a gamma distribution for spatial variations in cloud liquid. Fixing this inconsistency is a future goal.

Ice cloud optical properties are computed for each shortwave and longwave band used by the radiation code using a lookup table based on the modified anomalous diffraction approximation (Mitchell, 2002). The only input to these table lookups is ice effective radius, which is computed in P3. Because ice mass-density relationships are different for different size and riming regimes, ice effective radius is calculated via a table lookup described in Morrison and Milbrandt (2015). Because P3 merges the ice and snow categories used by traditional microphysics schemes into a single ice mode, radiation naturally acts on all frozen hydrometeors. Aerosol optical properties are specified in a lookup table as a function of wet refractive index and wet surface mode radius (Ghan & Zaveri, 2007).

Vertical overlap of partially-cloudy cells is accounted for by assuming maximum-random overlap (Geleyn & Hollingsworth, 1979) using the Monte Carlo Independent Column approach (MCICA Pincus et al., 2003).

## 2.7 Prescribed Aerosol

E3SMv1 uses a 4 Mode Aerosol Model (MAM4 Liu et al., 2016). For computational efficiency, we employ a version where this modal aerosol information is prescribed using monthly-average climatologies interpolated to the model grid from a  $1^\circ$  resolution E3SMv1 simulation. Implementation and use of prescribed-aerosol functionality is described in K. Zhang et al. (2013), Lebassi-Habtezion and Caldwell (2015), and Shi and Liu (2018). The default prescribed-aerosol implementation scales aerosols by different random perturbations every day to improve agreement between prescribed- and prognostic-aerosol simulations at high latitudes. These random daily jumps are confusing for analysis of short timeseries, so we've set the magnitude of random perturbations to zero for DYAMOND2. This might degrade aerosol behavior in polar regions.

Like E3SMv1, cloud condensation nuclei (CCN) concentration is derived from Abdul-Razzak and Ghan (2000). Ice nucleation follows Gettelman et al. (2010) for deposition nucleation and homogeneous freezing of solution droplets but retains the original P3 implementation for cloud and rain drop freezing.

## 2.8 Energy Fixer

SCREAM inherited its energy fixer from CAM. As described in Lauritzen and Williamson (2019), this energy fixer corrects errors due to pressure work, time integration in the dynamical core, inconsistent formulations of equation of state, and other minor sources of non-conservation. Historically, CAM and the atmospheric component of E3SM had used an incorrect formulation for energy. Williamson et al. (2015) documents this problem and provides a correction, which is used in SCREAM.

## 2.9 Timesteps

Like most atmosphere models, SCREAM's timestepping is a complex mixture of substepping and superstepping of individual processes. Ideally, model timesteps would be small enough that modest changes wouldn't have a noticeable effect on model behavior. Unfortunately, climate models have not yet reached that goal (Santos et al., 2020). Thus we list the timesteps used for the DYAMOND2 simulation in Table 1.

Main	Dycore	Dycore Remap	Advection	Radiation
75	9.375	18.75	75	300

**Table 1.** Timesteps used in SCREAM DYAMOND2 simulation (in sec). Processes not listed use Main timestep.

448

## 2.10 Tuning

449

450

451

452

453

454

455

456

457

458

459

460

461

462

Tuning is important for optimal performance of any weather or climate model, but should become less important at higher resolution where more processes are explicitly resolved and therefore expressed in a more complete and physical way. Because of time constraints and a reticence to tune away problems before understanding their source, the only parameter adjustment we made was to modify the lower limit of the eddy diffusivity damping timescale to get net top-of-atmosphere (TOA) radiation to match observations and to control surface temperatures under stable conditions at high latitudes. Because our tuning was based on short (1 or 2 day) simulations and therefore required comparison against higher-time frequency radiative observations which (as described in Sect. 4) have larger global-average bias than the monthly-average data used to assess the simulation-average radiation, the TOA net bias reported here still ended up being somewhat large. Our crude tuning approach also resulted in clouds which are too stratiform rather than convective (as described in Section 6.3). High latitude land surface temperature biases remain high, indicating that more tuning work is needed.

463

## 3 Experimental Design

464

465

466

467

468

469

470

471

The focus of this study is a 40 day global simulation (Jan 20 through Feb 28) performed as part of the DYAMOND2 intercomparison. Our implementation follows the guidance at <https://www.esiwace.eu/services/dyiamond/winter> as closely as practicable. Atmospheric initial conditions come from the European Center for Medium Range Weather Forecasting (ECMWF) Integrated Forecasting System (IFS) at its native 9 km grid spacing. Whereas some DYAMOND2 entrants are running with interactive ocean models, SCREAM is not yet able to do this. Instead we use SST at 6-hourly resolution as prescribed from IFS output smoothed by a 7 day running mean.

472

473

474

475

476

As mentioned in Sect. 2.7, aerosol distributions are prescribed from a 1° E3SMv1 simulation. This simulation was 6 years long with annually-repeating forcings (SST, sea ice extent, land use, solar forcing, aerosol emissions, greenhouse gases, and volcanic aerosols) values typical for the decade surrounding 2010. The last 5 years of this simulation are averaged to create a monthly varying aerosol field.

477

478

479

480

481

482

483

484

485

486

Soil and snowpack initial conditions were computed in 2 steps. First, the E3SM land model was run from Jan 1, 1979 through Aug 1, 2016 at the target resolution forced by observed atmospheric conditions from Version 7 of the Climatic Research Unit - National Centers for Environmental Prediction (CRUNCEPv7, Viovy (2018)) atmospheric forcing data. This simulation couldn't be extended beyond 2016 because of CRUNCEPv7 data availability. The second step was therefore to run from Aug 1, 2016 to Jan 20, 2020 using EAMv1 at 1° nudged to ERA5 reanalysis with a 6 hr timescale. Prescribed weekly SST and sea ice from OISSTv2 (Reynolds et al. (2002)) is used for this simulation. The machinery for this second step came from the Cloud-Associated Parameterizations Testbed (Phillips et al. (2004); Ma et al. (2015)).

Nodes	8x16 Dycore timing in minutes	8x16 with IO SDPD	8x16 without IO SDPD	16x8 without IO SDPD
1536	100.8	5.1	5.8	OOM
3072	53.9	8.6	10.3	OOM
4096	44.4	not run	not run	14.2
6144	29.2	14.2	19.2	23.1

**Table 2.** SCREAM timings as a function of KNL node count using either 8x16 MPI tasks vs OpenMP threads or 16x8 MPI tasks vs OpenMP threads per node. All timing runs were 1 day in length. Timings with IO include all standard output for our DYAMOND simulation. OOM means Out of Memory and IO stands for Input/Output.

#### 4 Observations for Evaluation

The short duration of this simulation and our focus on small time and spatial scales limit the range of observational datasets suitable for comparison. We rely heavily on the European Centre for Medium-Range Weather Forecasting’s ERA5 reanalysis (Hersbach et al., 2020). This retrospective simulation assimilates a massive array of observations, runs at 31 km horizontal resolution with 137 vertical levels and a top at 0.01 hPa, and is available at hourly resolution. Because model formulation strongly affects cloud and precipitation predictions from reanalysis, we use satellite products for cloud-related variables. In particular, we use half-hourly  $0.1^\circ$  gridded Global Precipitation Measurement (Hou et al., 2014, GPM) Integrated Multi-satellitE Retrievals for GPM (IMERG) product version V06B (G. J. Huffman & coauthors, 2019) for global precipitation. For radiative fluxes, we use CERES-EBAF  $1^\circ$  data averaged over February 2020 (Loeb et al., 2018). To examine the radiative properties of individual storms, we also use CERES-SYN hourly  $1^\circ$  data (Doelling et al., 2013, 2016). Cloud fraction and liquid water content are taken from CloudSat (Austin et al., 2009; Su et al., 2011) and from the CERES-CALIPSO-CloudSat-Merged product (Kato et al., 2010, C3M). CloudSat and C3M are not available for the 2020 dates simulated and are instead climatological averages.

Where possible, we compute long-term averages using the last 30 days of the simulation (Jan 30th through Feb 28th); we exclude the first 10 days of the run as spinup (though SCREAM fields stabilize after just one day of spinup, see Fig. 5). As noted above, some observational datasets are only available as monthly averages. For corresponding variables, we show results using just days in Feb. Finally, the first week or so of the simulation can be treated as a weather forecast, we use all 40 days of the simulation for some analysis of storm behavior.

#### 5 Performance

The DYAMOND2 simulation was performed as a series of 1536-node job submissions using the Knights Landing (KNL) nodes of Cori at the National Energy Research Supercomputing Center (NERSC). We found that using 8 MPI processes and 16 OpenMP threads per node provided the optimal balance of memory usage and performance for these 1536-node jobs. The overall throughput for the 40-day simulation, including I/O, was about 4-5 simulated days per day (SDPD). Further details about the performance of this 40-day DYAMOND2 simulation can be explored at <https://pace.ornl.gov/search/SCREAMv0.SCREAM-DY2.ne1024pg2.20201127>. As shown in Table 2, the model scales quite well - particularly in the dycore - and can achieve up to 23.1 SDPD without input or output (IO) on 6144 KNL nodes.

522 The simulation used the Software for Caching Output and Reads for Parallel I/O  
 523 (SCORPIO) library for reading input data and writing simulation output to the file sys-  
 524 tem. SCORPIO is derived from the Parallel I/O library (Hartnett & Edwards, 2021) and  
 525 continues to support the same application programming interface. To improve the I/O  
 526 write performance the library caches and rearranges output data between MPI processes  
 527 before using low level I/O libraries like the netCDF, Parallel netCDF (PnetCDF) (Latham  
 528 et al., 2003), and ADIOS (Godoy et al., 2020) libraries to write the data to the file sys-  
 529 tem. On Cori the simulation produced  $\sim 4.5$  TB of data per simulated day and achieved  
 530 an average I/O write throughput of  $\sim 2.5$  GB/s using the PnetCDF library.

531 Unsurprisingly for such a large run, we experienced several node failures during the  
 532 simulation requiring restarts from the previous day. Because E3SM is bit-for-bit repro-  
 533 ducible for identical initial conditions and forcings, these failures should not have any  
 534 impact on our results. During model development, we had problems with occasional ex-  
 535 tremely cold temperatures near the surface at wintertime high latitudes. We fixed this  
 536 problem by increasing turbulent diffusivity in stable atmospheric conditions, but this had  
 537 the side effect of increasing time-average warm bias in polar regions. The tuning used  
 538 here balances model stability against bias.

## 539 6 Results

### 540 6.1 Kinetic Energy Spectrum

541 At convection permitting resolutions, the simulated atmosphere’s kinetic energy  
 542 spectra recovers many features seen in observations and reveals many aspects of model  
 543 diffusion, filtering and parameterization behavior (Skamarock et al., 2014). As a first look  
 544 at this in SCREAM, we plot the horizontal kinetic energy power spectra at 250 hPa and  
 545 500 hPa in Fig. 2. The spectra are computed via spherical harmonic transforms of 3-hour  
 546 flow snapshots from days 22 and 23 of the simulation. We denote by  $E(k)$  the power of  
 547 the spherical harmonics of degree  $k$ . We plot compensated spectra,  $E(k)k^{5/3}$ , to better  
 548 illustrate the high wave number  $k^{-5/3}$  regime. SCREAM reproduces the observed Nastrom-  
 549 Gage transition from a  $k^{-3}$  scaling at low wavenumbers to a  $k^{-5/3}$  regime (Nastrom &  
 550 Gage, 1985; Lindborg, 1999). The  $k^{-5/3}$  region extends to  $\sim 6\Delta x$  wavelength (wavenum-  
 551 ber 2000), where the spectra start to roll off and become dominated by model diffusion.  
 552 Thus SCREAM’s effective resolution is similar to ICON and IFS (Neumann et al., 2019)  
 553 despite SCREAM’s novel use of a coarser grid for physical parameterizations.

### 554 6.2 General Features

555 Global-average model biases are modest in size but are generally larger than the  
 556 range of observed day-to-day variability within the simulation period (Fig. 3). TOA net  
 557 shortwave (SW) radiative absorption  $SW_{\text{net}}$  and longwave (LW) emission  $LW_{\text{net}}$  are both  
 558 too strong but (as noted in Section 2.10) were tuned to compensate each other such that  
 559 TOA radiative bias  $rad_{\text{net}}$  exhibits only a modest warming tendency. Radiative biases  
 560 are almost entirely due to clouds rather than clear-sky bias (not shown). Too little  $SW_{\text{net}}$   
 561 reflection and excessive  $LW_{\text{net}}$  emission suggests a lack of clouds, so it is surprising that  
 562 model calculated vertically-projected cloud fraction is 5% too large. This is an unfor-  
 563 tunate result of using a RH-based ice cloud fraction parameterization without retuning  
 564 for higher resolution. As a result, large cloud fraction occurs in cold regions which don’t  
 565 necessarily have cloud mass (Fig. 4). Fortunately, ‘clouds’ without condensate are treated  
 566 like clear-sky air by radiation, so our mistake is mostly cosmetic in nature. In the fu-  
 567 ture we intend to switch to a mass-based all-or-nothing ice cloud fraction scheme to avoid  
 568 this problem. An offline version of this mass-based approach (shown in Fig. 4) is used  
 569 in the remainder of this paper wherever upper-level cloud fraction is required.

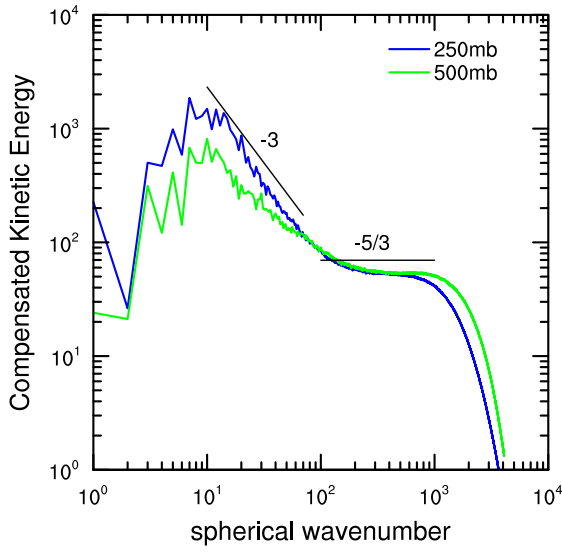


**Figure 2.** Compensated kinetic energy spectra ( $E(k)k^{5/3}$ ) at 500 hPa and 250 hPa from days 23-24 of the simulation. The black lines show idealized  $E(k) \approx k^{-3}$  and  $E(k) \approx k^{-5/3}$  scalings. See text for details.

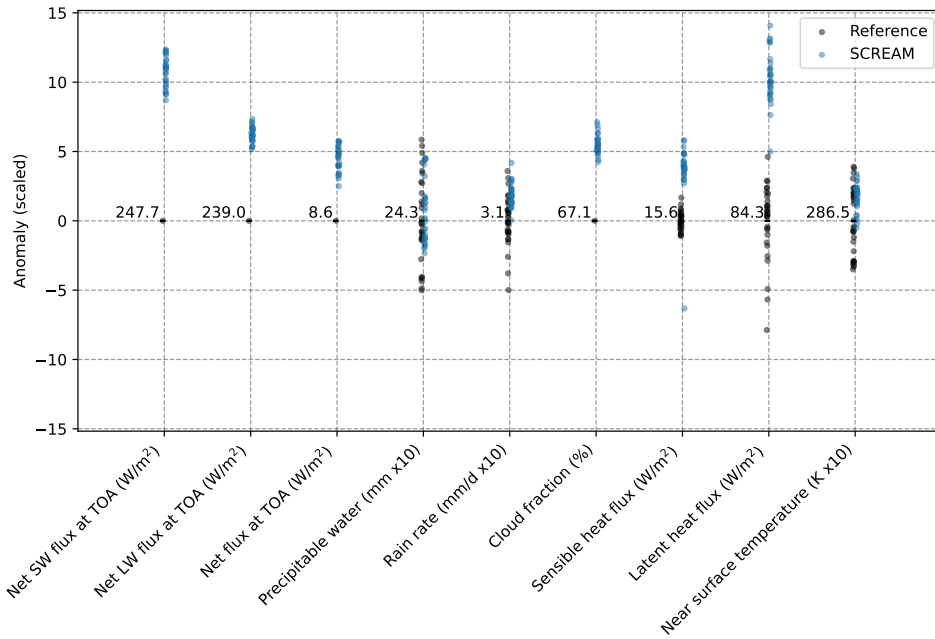


**Figure 3.** Global-mean anomaly in variables listed along x-axis. Anomalies are calculated relative to the February 2020 average of CERES-EBAF (for radiative fluxes and cloud fraction), and the January 30 2020 through Feb 28 2020 average of ERA5 (for precipitable water, sensible and latent heat fluxes, and near surface temperature), and GPM (for precipitation). Each dot represents a single daily average, so vertical spread gives a sense of temporal variability. There is a dot for each day in Feb 2020. Units for each variable are included in the x-axis labels.

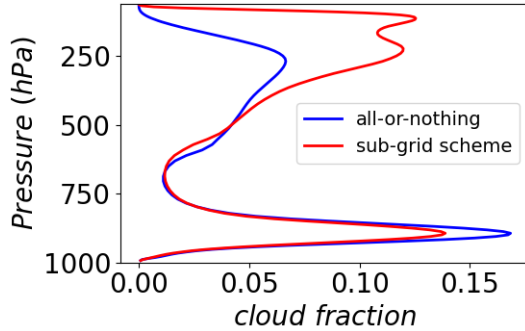


**Figure 4.** Vertical profile of Feb-mean tropics-averaged ( $30^{\circ}\text{S}$ - $30^{\circ}\text{N}$ ) cloud fraction computed by SCREAM compared to an offline calculation of cloud fraction based on assuming an entire cell is saturated whenever cloud water content  $> 10^{-5} \text{ kg kg}^{-1}$ .

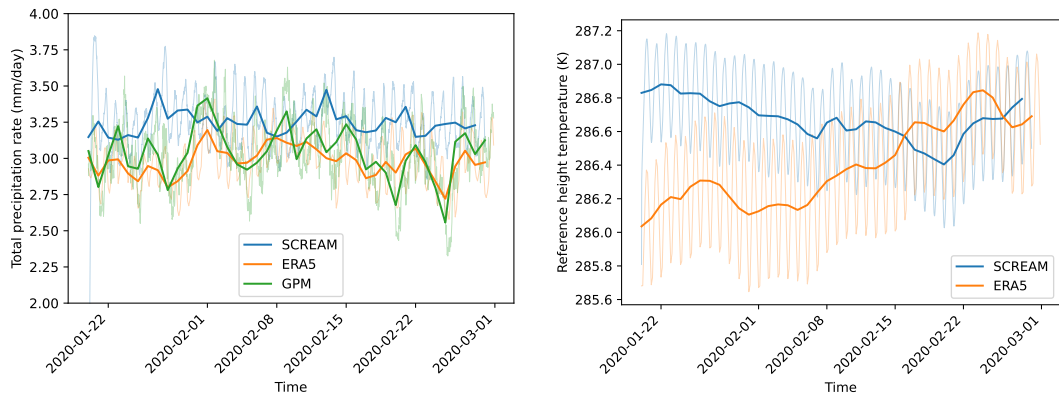


**Figure 5.** 15 minute (thin curves) and daily-mean (thick curves) time series of global-average precipitation (left) and 2 m temperature (right) for the duration of the DYAMOND2 simulation.

570 Global-average precipitation is  $\sim 0.3 \text{ mm day}^{-1}$  larger in SCREAM than GPM, which  
 571 is consistent with a general tendency for models to have higher precipitation rates than  
 572 observations (Terai et al., 2018), including in the previous DYAMOND intercomparison  
 573 (Stevens et al., 2019). Temperature at 2 m height (T2m) and vertically-integrated va-  
 574apor lie within observed day-to-day variability in the global average, though we show later  
 575 that this is due in part to compensating errors. Sensible heat flux (SHF) and surface evap-  
 576 oration (a.k.a. latent heat flux; LHF) are larger than observed, probably due to near-  
 577 surface wind speed biases discussed later.

578 Fig. 5 demonstrates that our simulation doesn't drift rapidly in time, even in the  
 579 first few days of the run. Time tendencies in other key variables are likewise small (not  
 580 shown). The amplitude of global-average diurnal variations is also reasonable. Interest-  
 581 ingly, GPM and ERA5 contain periods where global-average precipitation drops, while  
 582 SCREAM is more temporally invariant. Understanding what causes these global-average  
 583 drops is an interesting question for future work.

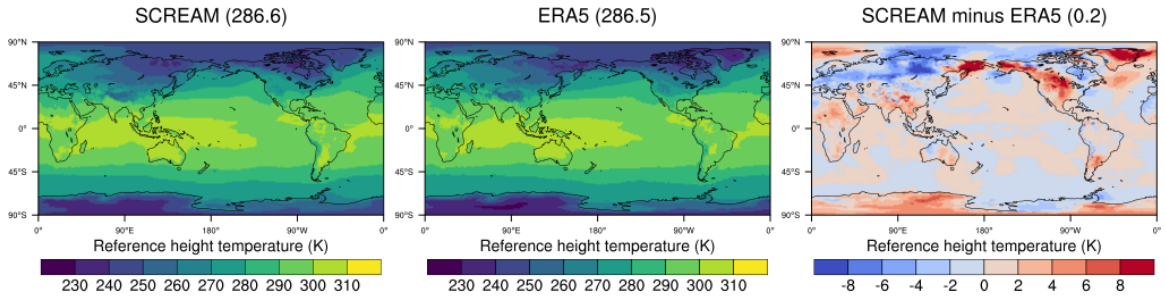


**Figure 6.** Near-surface temperature averaged over Jan 30 through Feb 28, 2020 from SCREAM and ERA5 reanalysis.

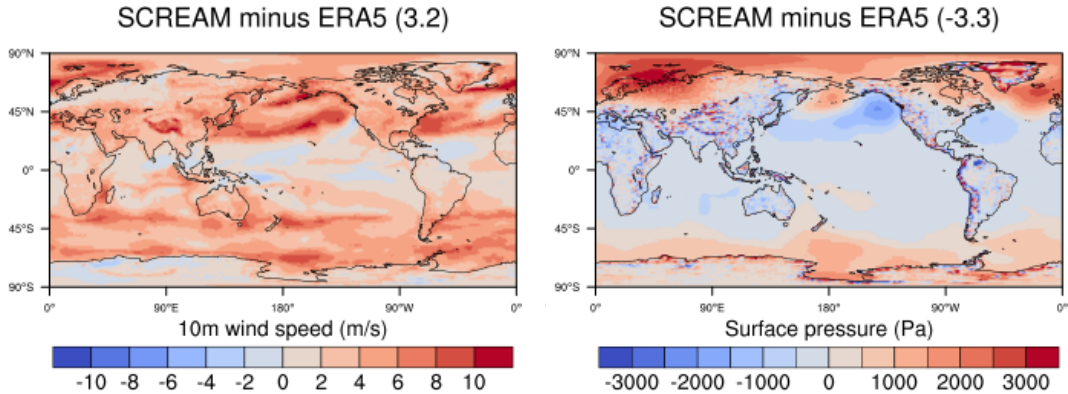


**Figure 7.** Bias (relative to ERA5) in 10 m wind speed (left) and surface pressure (right) averaged over the last 30 days of the simulation.

584 Near-surface temperature biases are modest at low latitudes and larger at high latitudes (Fig. 6). In the first few days of our simulation, T2m was uniformly too high at  
 585 high latitudes (not shown), which we attribute to a land initial condition created by driv-  
 586 ing our land model with a 1° atmosphere model which one might expect to handle snow-  
 587 pack poorly. We tuned overturning turbulent mixing in stable conditions to compensate  
 588 the warm biases we saw in our initial short testing runs; it appears in retrospect that  
 589 we overdid it. Averaged over the last 30 days of the simulation, the US, Greenland, and  
 590 the far eastern side of Russia retain >6 K warm biases, while north Asia and the Cana-  
 591 dian Arctic are ~5 K too cold. Improving these temperature biases is a future goal. Sur-  
 592 face pressure is also too large at high latitudes (right-hand panel of Fig. 7), which will  
 593 translate (through thermal wind balance) to errors in wind speed.  
 594

595 Near-surface wind speed is too high almost everywhere but particularly over mid-  
 596 latitude oceans (Fig. 7). Bias is smallest in the tropics. We are still working to under-  
 597 stand and fix this deficiency, but note that switching to the Zeng et al. (2002) scheme  
 598 significantly alleviates excessive wind speeds. Consistently positive wind bias is solely  
 599 a feature of the surface layer - even at 925 hPa wind biases are much more balanced around  
 600 zero. Overall, it is surprising that so many aspects of our simulation look quite good in  
 601 spite of this near-surface wind bias. Overly strong SHF and LHF mentioned earlier are  
 602 unsurprising given strong near-surface wind speed.

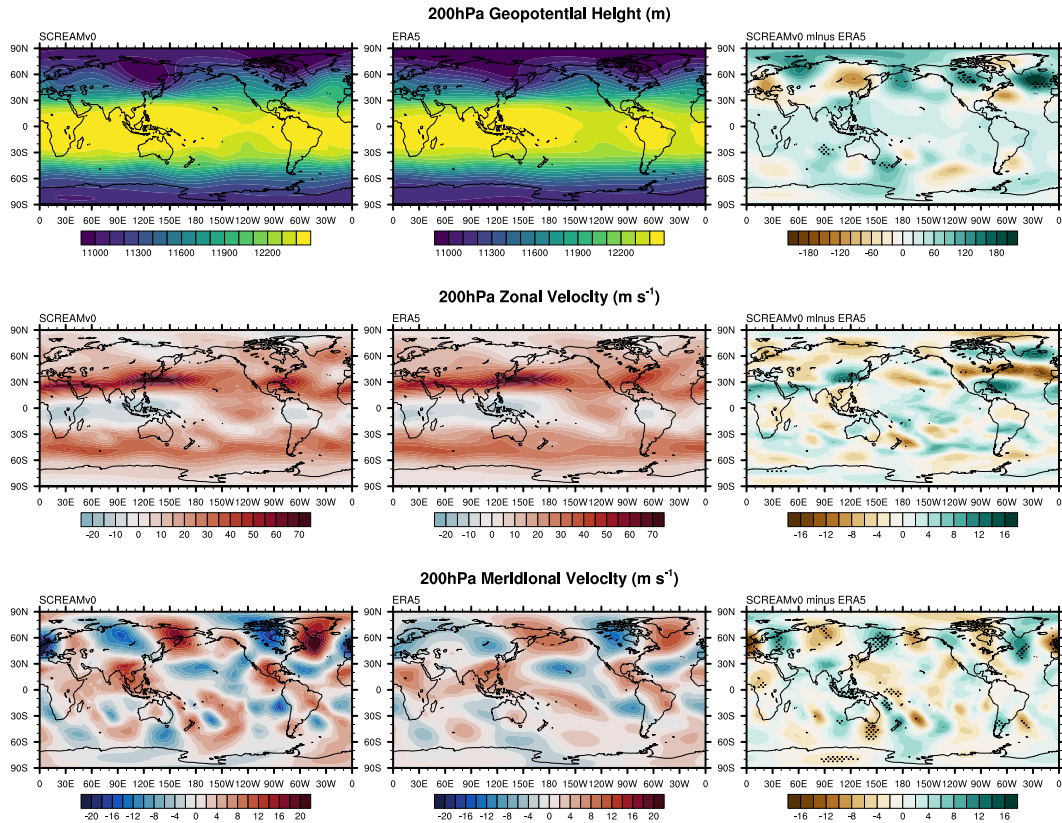


**Figure 8.** 200hPa geopotential height (top), zonal wind speeds (middle), and meridional wind speeds (bottom) averaged over the last 30 days of the simulation. Stippling in the difference plots (right panels) indicates regions where SCREAM falls outside the range of mean values for all years in ERA5 1979-2020.

603 Fig. 8 shows geopotential height and wind speeds on the 200hPa pressure surface  
 604 averaged over the period from January 30th to February 28th. Although there is gener-  
 605 ally strong agreement between SCREAM and ERA5, two hotspots emerge. First, the  
 606 wintertime Rossby wave train that reinforces the upper-level trough over Greenland is  
 607 markedly more intense in SCREAM than in ERA5. The result is southward displace-  
 608 ment of the subtropical jet (STJ) over the West Atlantic and anomalously strong pole-  
 609 ward flow from the STJ towards Greenland. In fact, this anomaly in the Central Atlantic  
 610 is largely barotropic, present even at 850hPa with approximately the same magnitude  
 611 (not shown). A second region of anomalous behavior also exists around the periphery  
 612 of Australia where the 200hPa geopotential surface is enhanced, producing spurious merid-  
 613 ional flow throughout this region. Notably, the bias pattern present in the difference plots  
 614 suggest an enhancement in wavenumber 4 in both hemispheres centered around the loca-  
 615 tions of cubed-sphere corners in the dynamics grid. The bias appears slightly stronger  
 616 in the first 20 days of the simulation than the last 20 days (not shown). The source of  
 617 this behavior is under investigation.

### 618 6.3 Radiation and Clouds

619  $SW_{net}$  and  $LW_{net}$  radiation biases were found in Fig. 3 to somewhat cancel in the  
 620 global mean; Fig 9 reveals that this cancellation also holds regionally in many places.  
 621 Cancellation between SW and LW biases is a hallmark of high clouds. Further evidence

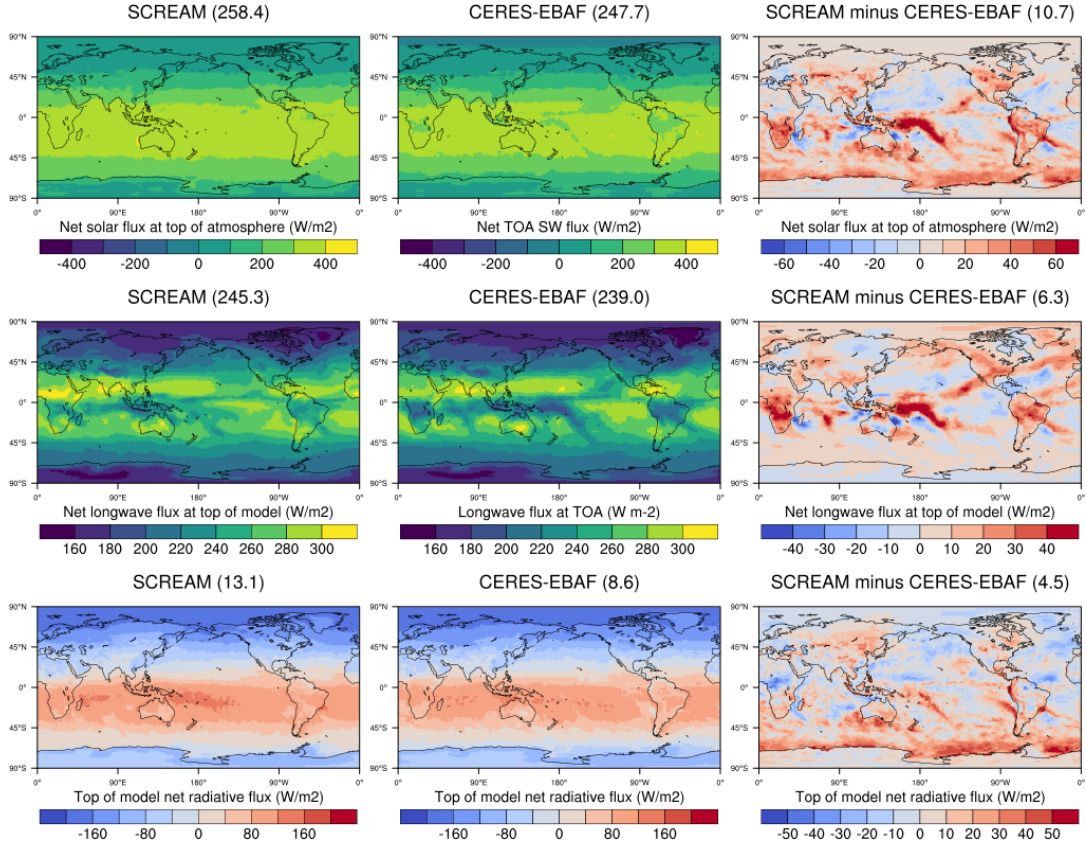


**Figure 9.** TOA radiation averaged over February 2020. Top is SW ( $>0$  warms the planet), middle is LW ( $>0$  cools the planet), and bottom is net ( $>0$  warms the planet).

622 of problems with high clouds is the pattern of  $LW_{net}$  bias, which is large where deep con-  
 623 vective clouds are expected.

624 Fig. 10 explores the vertical profile of tropical clouds compared to climatological  
 625 CloudSat measurements. Because SCREAM results are for one month only, detailed com-  
 626 parison is not appropriate. Nonetheless, SCREAM’s ability to capture the general fea-  
 627 tures from CloudSat data is very good, particularly compared to the (albeit old) GCMs  
 628 analyzed in Su et al. (2011). In particular, SCREAM captures the bimodality of deep  
 629 and shallow clouds and does a reasonable job of matching the quantitative magnitude  
 630 of each peak. Ability to better capture the structure of tropical convection is perhaps  
 631 unsurprising given that resolving such convection was a primary motivation for devel-  
 632 oping a 3.25 km model. Both simulated cloud peaks sit lower in the atmosphere than  
 633 they do in the measurements. Another notable deficiency in SCREAM is the lack of mid-  
 634 level clouds, which may be tied to either the absence of significant cloud detrainment at  
 635 mid-levels, overly efficient sedimentation of cloud particles through mid-layers, or both.  
 636 Reasonable or even excessive SCREAM anvil condensate in Fig. 10 and erroneously large  
 637 high cloud fraction in Fig. 4 are at odds with excessive LW emission to space in Fig. 9.  
 638 We are still working to understand this conundrum.

639 Net outgoing radiation over the northern hemisphere oceans is found in Fig. 9 to  
 640 be too strong in general (i.e. the oceans in Fig. 9i are colored blue indicating more ra-

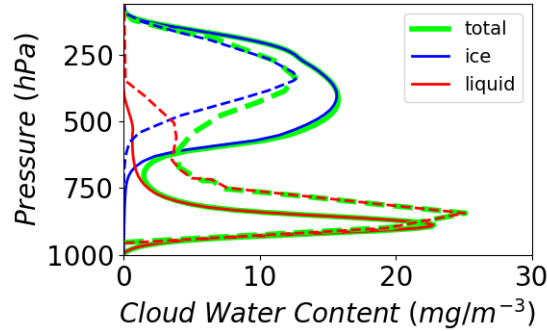


**Figure 10.** Cloud water content (CWC) profiles from SCREAM (solid) versus CloudSat observations from Su et al. (2011) (dashed). Data are averaged over all longitudes and latitudes between  $30^{\circ}\text{S}$ - $30^{\circ}\text{N}$  and over all 40 simulated days.

641 diation leaving than entering the atmosphere). This is due mainly to trapping of LW emis-  
 642 sion;  $\text{SW}_{\text{net}}$  insolation at higher northern latitudes is too small in wintertime to matter.

643 Away from high-latitude winter regions, the impacts of high clouds on  $\text{SW}_{\text{net}}$  and  
 644  $\text{LW}_{\text{net}}$  tend to cancel so  $\text{rad}_{\text{net}}$  is a good indicator of lower-level cloudiness. Fig. 9 re-  
 645 veals a lack of low clouds over the southern ocean, but generally decent low-cloud radi-  
 646 ative forcing in the stratocumulus decks off the west coast of the continents. Anemic stra-  
 647 tocumulus is a perennial GCM bias (Nam et al., 2012; Jian et al., 2020), so capturing  
 648 this cloud type in SCREAM is exciting. This is particularly surprising since 3.25 km grid  
 649 spacing is generally considered insufficient to capture boundary-layer clouds like this. One  
 650 potential reason for improvement is our higher-order turbulence closure. Increased ver-  
 651 tical resolution ( $\sim 50$  m in the boundary layer) in addition to SCREAM’s high horizon-  
 652 tal resolution also likely helps; Bogenschutz et al. (2021) and Lee et al. (2021) demon-  
 653 strate that increased vertical resolution helps to ameliorate these biases in E3SM, ow-  
 654 ing to better representation of the cloud top cooling and turbulence feedback, but both  
 655 studies hypothesize that concurrent increases in the horizontal and vertical resolution  
 656 are needed to adequately simulate the coastal Sc. Results with SCREAM support that  
 657 hypothesis.

658 Figures 11a-b display the February 2020 average profiles of cloud fraction and cloud  
 659 liquid water for SCREAM and the February 2006-2010 climatology from C3M. These  
 660 profiles are averaged over a small domain neighboring the coast of Peru and Chile. This  
 661 domain was selected as it represents the area of most intense shortwave cloud radiative  
 662 effect (SWCRE) biases associated with low clouds in the northern-hemisphere winter sea-  
 663 son for standard-resolution GCMs (e.g. Golaz et al. (2019); Danabasoglu et al. (2020)).  
 664 Although different averaging periods are used for C3M versus SCREAM data, stratocu-  
 665 mulus are a persistent feature in this region so broad comparison is reasonable. SCREAM  
 666 produces cloud structure quite similar to the observations. Though SCREAM cloud frac-  
 667 tion in Fig. 11a may appear to be underrepresented, we note that its deficiencies are small  
 668 compared to most GCMs (Bogenschutz et al., 2021). In addition, cloud liquid water in  
 669 Fig. 11b matches observations almost perfectly. Fig. 11c depicts a snapshot of the SWCRE  
 670 on 01 March, 2020 at 18:00:00 UTC from SCREAM to demonstrate the model’s abil-  
 671 ity to simulate healthy coastal Sc cloud decks and the gradual transition to more bro-  
 672 ken cloud.

673 Fig. 12 displays the temporally-averaged curtain of cloud fraction along the  $20^{\circ}\text{S}$   
 674 transect across the stratocumulus-to-deep-convection transition for SCREAM February

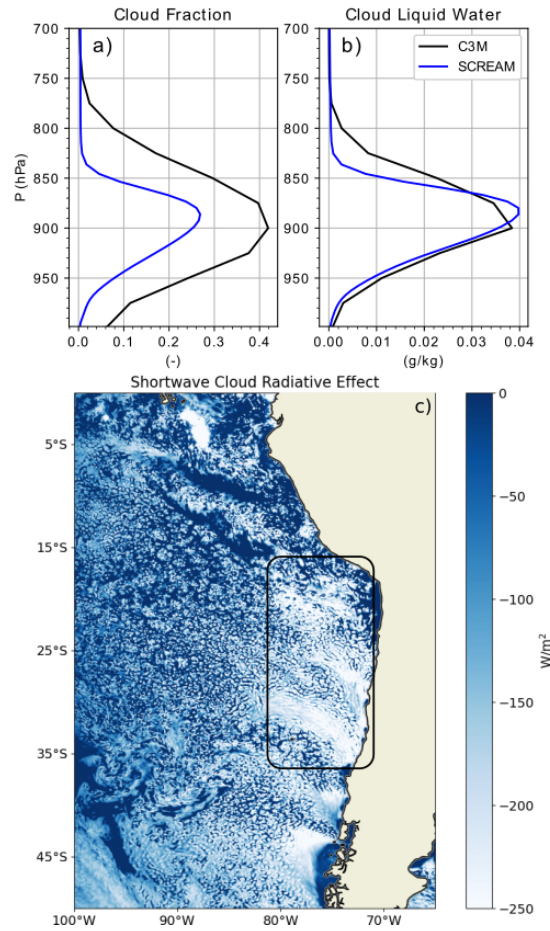


**Figure 11.** Temporally and spatially averaged profiles of cloud fraction (a) and cloud liquid water (b) for SCREAM and C3M. SCREAM profiles are averaged for the month of February 2020 while the C3M represents the February climatology from 2006-2010. Both SCREAM and C3M profiles represent spatial averages from the southeast Pacific coastal stratocumulus region bounded from 35°S to 15°S and 275°E to 290°E. The area used for spatial averaging is denoted in (c), which represents a snapshot of shortwave cloud radiative effect from SCREAM for 01 March 2020 at 18:00:00 UTC.

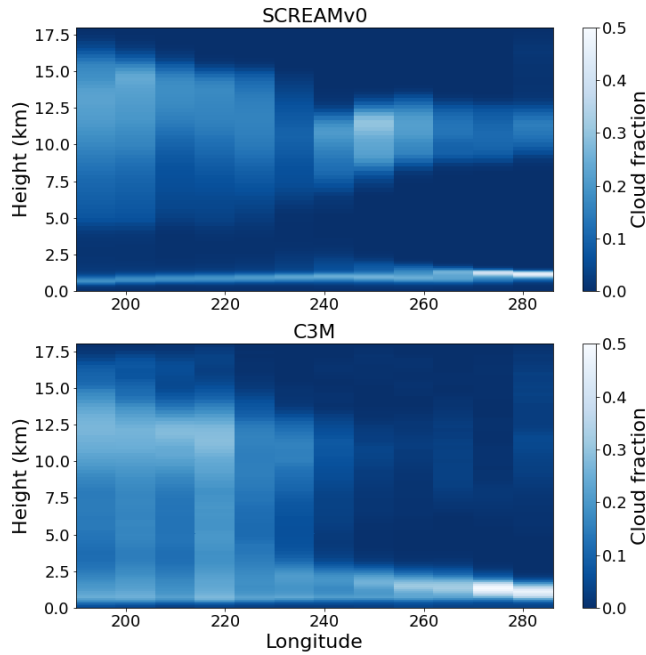


**Figure 12.** Temporally-averaged curtain of cloud fraction along the 20°S transect across the stratocumulus to deep convection transition. SCREAM clouds are averaged over the month of February 2020 while the C3M represents the February climatology from 2006-2010. Both SCREAM and C3M profiles represent curtains bounded from 24°S to 16°S.

2020 average and C3M February climatology from 2006-2010. When read from right to left (i.e. along the direction of prevailing easterly winds), C3M observations depict a gradual deepening of cloud in the lower troposphere over progressively warmer SSTs. SCREAM looks reasonable near the coast but fails to deepen to the W and is generally too thin in depth and too weak. This was an unintended consequence of tuning choices made in the SHOC parameterization to achieve reasonable radiation balance; further tuning since this simulation has improved the realism of trade cumulus.

#### 6.4 Precipitation

Evaluating the spatial distribution of precipitation from a 40 day simulation is challenging. Forty days is too long for comparison against weather events but too short to average out the effects of individual storms. Zonal-averaging beats down some of this weather noise and large-scale tropical precipitation structure is probably robust, but results should still be taken with caution. In Fig. 13, zonal-average precipitation is found to generally agree well with both GPM and ERA5 except for excessive rainfall on the equatorward side of the northern-hemisphere storm track and at the poleward edges of the tropics. GPM is known to be biased low at higher latitudes due to problems detecting light rain and snow (G. Huffman et al., 2019), which might partially explain storm track and polar biases. Fig. 14 shows that tropical zonal-mean bias is due to a complicated mixture of differences in the meridional structure of precipitation. SCREAM tends to have stronger precipitation on the east side of land masses, in particular over the Maritime Continent (which has been a long-standing bias in E3SM; Golaz et al., 2019) and

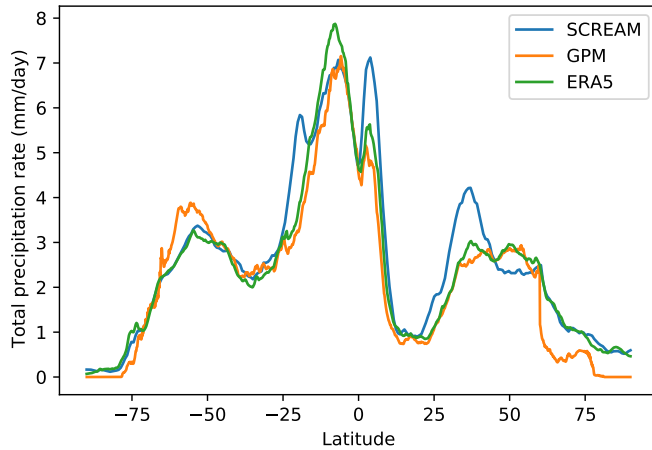


**Figure 13.** Zonal-average precipitation averaged over the last 30 days of the SCREAM simulation.

696 west of Madagascar. Heavy precipitation in the ITCZ extends too far east, which is another  
 697 persistent E3SM bias. Precipitation in the South Pacific Convergence Zone (SPCZ) is, on the other  
 698 hand, too weak and a bit too zonal. This may indicate that SCREAM (like most climate models)  
 699 suffers from double-ITCZ problems (Li & Xie, 2014). Precipitation over the Amazon rain forest  
 700 is slightly too strong, which is the opposite from what is seen in conventional climate models  
 701 (Yin et al., 2012).

702 A great success of cloud-resolving models are their ability to simulate the diurnal cycle of  
 703 precipitation (Khairoutdinov et al., 2005; Sato et al., 2009; Stevens et al., 2019). This is a  
 704 feature which coarser resolution models struggle with (Covey et al., 2016), though progress  
 705 has been reported (Xie et al., 2019). As documented in Fig. 15, SCREAM is able to capture  
 706 the morning-time peak over the oceans and late afternoon peak over land. The diurnal cycle  
 707 over the Maritime Continent and Madagascar - two areas dominated by sea breezes - is actually  
 708 stronger than observed in GPM (but is weaker in magnitude than TRMM’s observed climatology;  
 709 not shown). Stronger diurnal amplitude in these areas is perhaps unsurprising given that daily  
 710 mean precipitation was also noted to be too high in these regions.  
 711

712 Like conventional GCMs (Stephens et al., 2010; Na et al., 2020), SCREAM has a tendency  
 713 towards having too much drizzle and not enough strong precipitation (Fig. 16). The magnitude  
 714 of this bias is, however, much smaller than typically found in conventional GCMs (e.g. Caldwell  
 715 et al. (2019) Fig. 12). Thus we consider simulation of heavy precipitation to be a victory for  
 716 SCREAM.

717 Hovmöller diagrams showing precipitation averaged from 5° N to 5° S latitude as a function  
 718 of longitude and time are useful for evaluating the temporal intermittency and propagation of  
 719 tropical convection which collectively result in the Madden-Julian Oscillation (MJO; (Madden &  
 720 Julian, 1971)). Usually MJO analyses filter out signals outside of a 20-90 day window, but  
 721 our 40 day simulation precludes such processing. A longer simulation is needed for statistical  
 722 robustness, but it seems clear in Fig. 17 that SCREAM triggers convection too frequently. This  
 723 feature is also apparent in instantaneous snapshots of precipitation, water vapor, and cloud mass  
 724 (not shown). We are still investigating the source of this “popcorn convection”, which also  
 725 appears in other convection-permitting regional and global models (Arnold et al., 2020;  
 726 Kendon et al., 2012). As found for other GCPMs (Miura et al., 2007; Miyakawa et al.,  
 727 2014), SCREAM does a good job of propagating convective events eastward, though its  
 728 propagation speed is perhaps slightly fast.

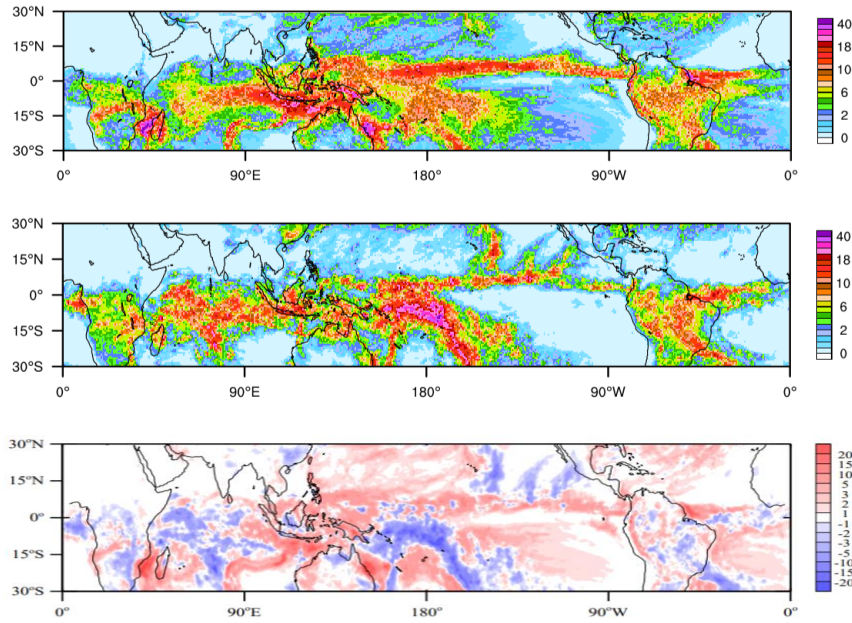


**Figure 14.** Tropical precipitation over the last 30 days of the SCREAM run (top), GPM observations averaged over the same period (middle), and their difference (SCREAM minus GPM, bottom).

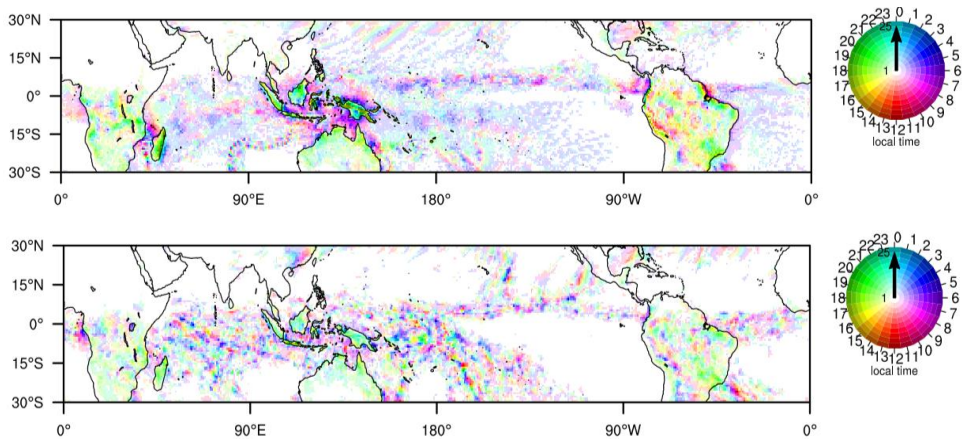


**Figure 15.** Diurnal cycle of precipitation averaged over the last 30 days of the SCREAM run (top) and GPM observations (bottom). Hue indicates time of peak precipitation and intensity indicates diurnal amplitude. Amplitudes less than  $1 \text{ mm day}^{-1}$  are colored white and colors saturate at  $25 \text{ mm day}^{-1}$ .

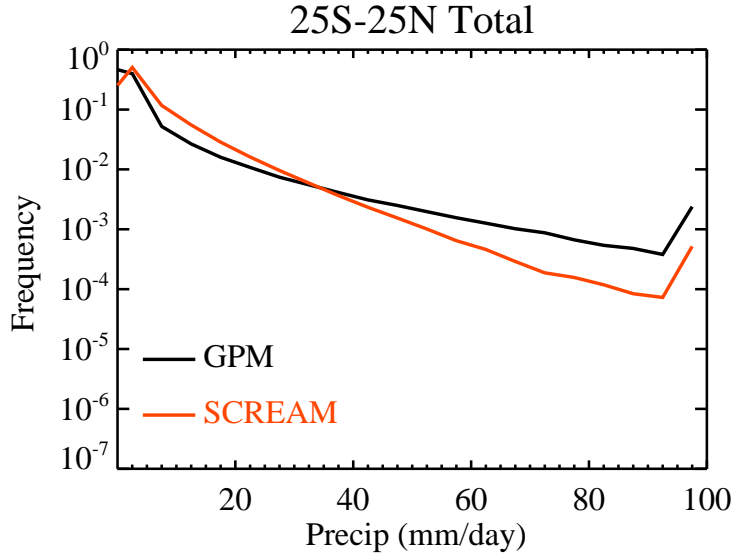


**Figure 16.** Histogram of tropical precipitation over the ocean for the last 30 days of the SCREAM simulation compared to equivalent days from GPM.

729 The statistical analysis of precipitation above is important, but it ignores the fact  
 730 that precipitation comes from storms whose characteristics vary regionally. The next few  
 731 subsections explore SCREAM’s treatment of important storm types.

## 732 6.5 Tropical Cyclones

733 Tropical cyclones (TCs) are some of the most intense storms in the world, combin-  
 734 ing intense precipitation with winds frequently in excess of  $30 \text{ m s}^{-1}$ . Although some global  
 735 models are able to represent TC frequency and intensity well at  $0.25^\circ$  grid spacing, re-  
 736 solving the inner structure of these storms requires much finer resolution (Wehner et al.,  
 737 2014; Zarzycki & Jablonowski, 2015; Judt et al., 2021). A key advantage of running global  
 738 convection-permitting models is the ability to represent and study multiscale interactions  
 739 between the inner structure of tropical cyclones and the large-scale environment (Satoh  
 740 et al., 2019). In the first phase of the DYAMOND project, models produced a wide range  
 741 of tropical cyclone counts and intensities with counts as low as 4 to as high as 20, while  
 742 in reality there were 14 (Stevens et al., 2019; Judt et al., 2021). In this section, we pro-  
 743 vide a brief and broad overview of the tropical cyclones identified in the SCREAM sim-  
 744 ulation.

745 Fig. 18 shows TC tracks during the simulation period from SCREAM, ERA5, and  
 746 IBTrACS observations (Knapp et al., 2010, 2018). SCREAM and ERA5 tracks are com-  
 747 puted using the TempestExtremes (TE) algorithm and the criteria described in appendix  
 748 A1, while IBTrACS are based on expert judgement. Large discrepancies between IBTrACS  
 749 and reanalysis datasets highlight the importance of using consistent criteria to classify  
 750 storms. Note as well that the chaotic nature of weather means that storms later in the  
 751 SCREAM simulation are not expected to match those found in ERA5 or in observations.  
 752 Within the days of potential predictability (up to two weeks), one TC exists in both the  
 753 SCREAM simulation and ERA5 data (Moderate Tropical Storm Diane). Another storm  
 754 that is present in ERA5 (Moderate Tropical Storm Esami) does not organize in SCREAM,  
 755 although a weak low pressure region does persist. Over the entire simulation period, we  
 756 identify five tropical cyclone tracks in SCREAM during the 40 day simulation and six

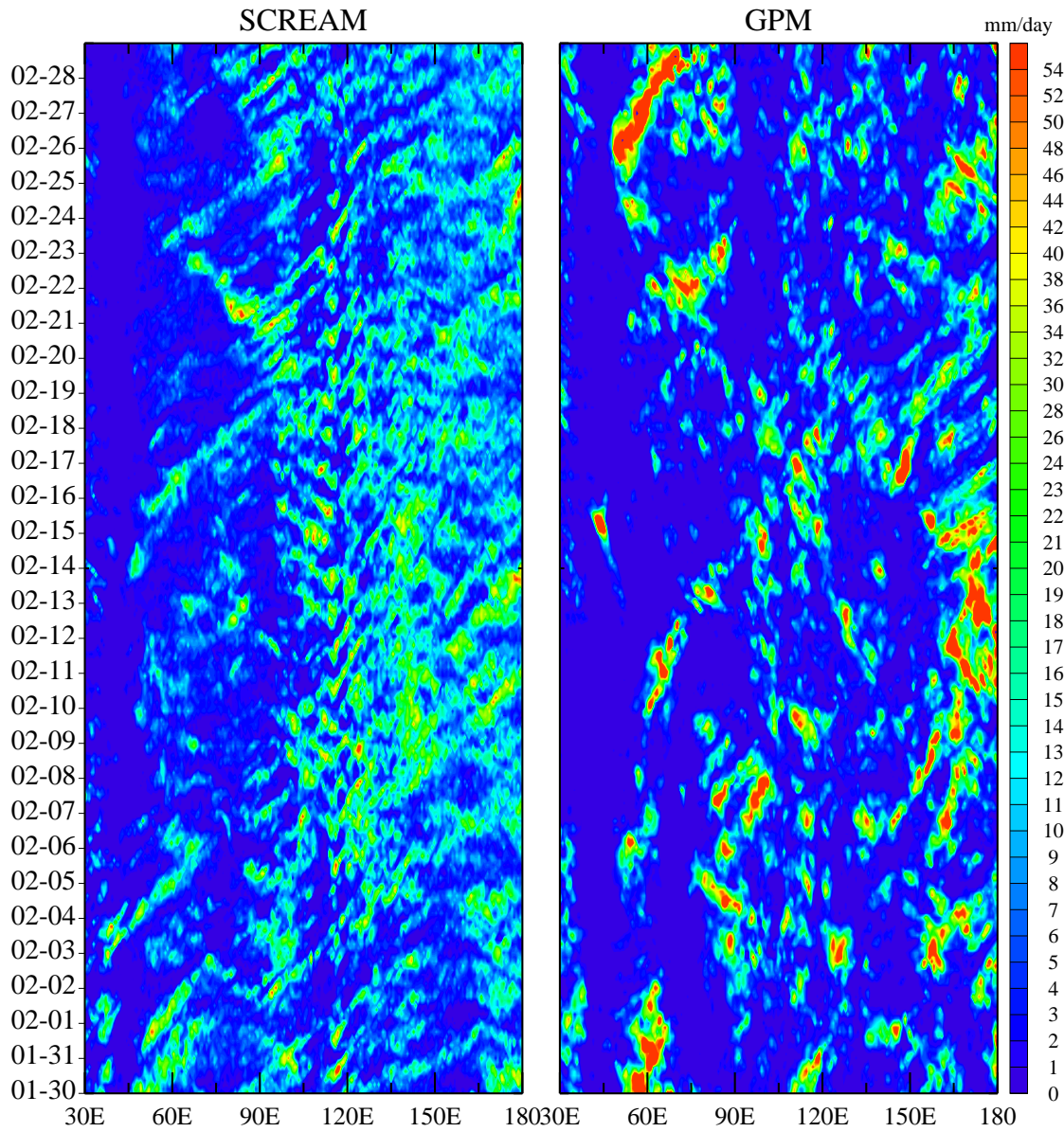


**Figure 17.** Precipitation averaged from  $5^{\circ}$  N to  $5^{\circ}$  S as a function of longitude (x-axis) and time (y axis) from SCREAM (left) and GPM precipitation observations (right).

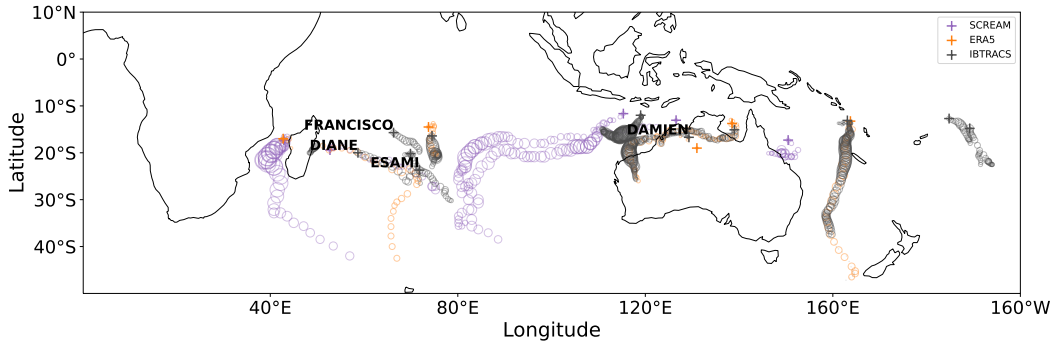


**Figure 18.** Tracks of tropical storms from IBTrACS (grey) and identified by the Tempest Extremes algorithm in SCREAM (purple) and in ERA5 (orange) between Jan 20 and Feb 28, 2020. Starting location is indicated with a plus (+).

757 tracks in the ERA5 reanalysis data. All five TCs in SCREAM occur in the Southern Hemi-  
 758 sphere, with four over the Indian Ocean and one off the northwestern coast of Australia  
 759 over the Pacific Ocean, all broadly located where TCs are found in the reanalysis.

760 In ERA5, Diane starts off as a tropical depression with central pressure of 1020 hPa,  
 761 but its pressure drops down to 990 hPa by Jan 26 with sustained maximum winds of 25  
 762 m/s (49 knots) or more. The simulated storm track from SCREAM closely follows that  
 763 found in the reanalysis (Fig. 19a), although it forms farther to the east and moves east-  
 764 ward more slowly. The maximum wind speed within a  $6^\circ \times 6^\circ$  box around the storm is  
 765 also higher in the model, but this is likely due to the use of native grid data in SCREAM  
 766 and the coarser regridding of the reanalysis data. Precipitation rates in SCREAM and  
 767 reanalysis closely follow each other until ERA5 starts tapering off while SCREAM con-  
 768 tinues growing. GPM precipitation, however, includes a period of much stronger precipi-  
 769 tation which isn't captured by either model simulation. Interestingly, SCREAM has a  
 770 strong and regular diurnal cycle of precipitation which isn't found in the other timeseries.  
 771 Although the data for this storm from IBTrACS spans a much shorter period in the storm  
 772 lifetime than identified by Tempest Extremes from either the reanalysis or the SCREAM  
 773 simulation, the magnitudes of central pressure and maximum 10-m wind speed are in  
 774 good agreement between SCREAM, ERA5, and IBTrACS for the period that does over-  
 775 lap.

776 Because Severe Tropical Storm Diane does not fully develop a canonical tropical  
 777 cyclone structure and exhibits hurricane force winds only for a few hours, we take a more  
 778 detailed look at a stronger storm in the model which forms on Feb 10 and produces sur-  
 779 face wind speeds which classify it as a category 3 hurricane (Fig. 19g). For reference,  
 780 the storm's maximum intensity (based on minimum surface pressure values) is the me-  
 781 dian of the five storms tracked in SCREAM (not shown). Fig. 19e shows the cyclone track,  
 782 which spans sixteen days. The surface pressure rapidly drops from Feb 11 to Feb 14, a  
 783 minimum pressure of 930 hPa on Feb 16, when maximum 10-m wind speeds are also reached.  
 784 By that point, the storm has formed a distinctive eye, ringed by strong precipitation rates  
 785 reaching 100 mm/hr and wind speeds greater than 60 m/s (Fig. 20). The high surface  
 786 wind speeds drive surface latent heat fluxes greater than  $500 \text{ W m}^{-2}$ , and a vertical north-  
 787 south curtain centered on the point of minimum surface pressure shows the boundary  
 788 layer flow is transporting energy towards the eye, particularly in the southern half of the  
 789 storm (Fig. 20).

790 More analysis is necessary for an in depth study of the storm characteristics in SCREAM,  
 791 as was done by Judt et al. (2021) for the models participating in the first phase of DYA-

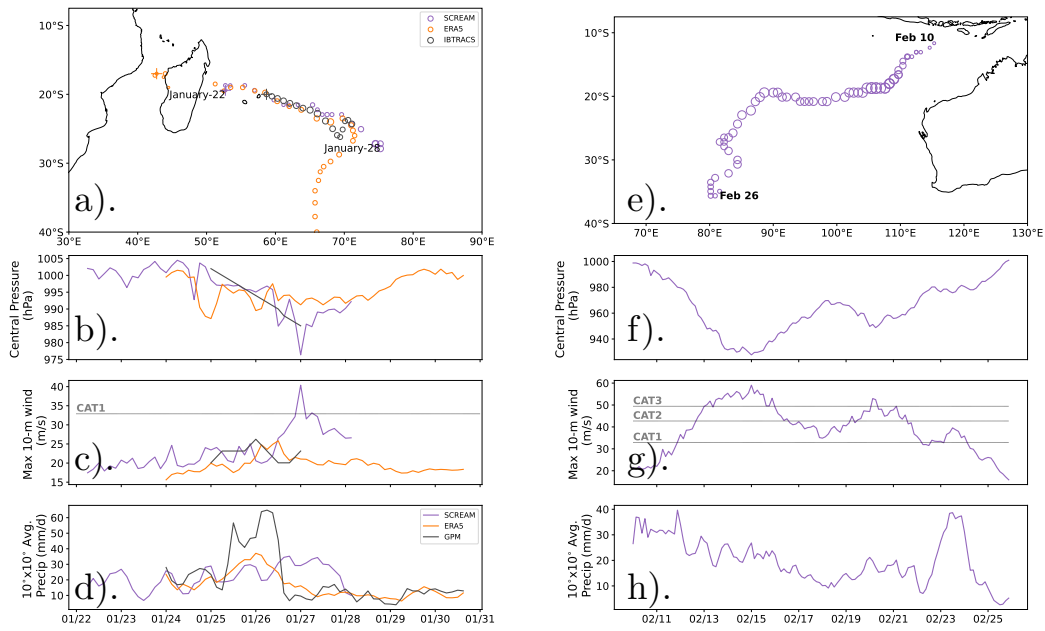


**Figure 19.** (a) Tracks of the tropical storm Diane from IBTrACS (grey) and as identified by the Tempest Extremes algorithm in SCREAM (purple) and in ERA5 (orange). Starting location is indicated with a + symbol. Shown below the tracks are time evolution of the storm’s minimum central pressure (b), maximum 10-m wind speeds within  $5^\circ$  of the storm center (c), and area-averaged precipitation rate (d). (e-h) Same as (a-d) but for Feb 10 tropical cyclone in SCREAM simulation. No observational equivalent is shown, because it is outside the period of predictability.

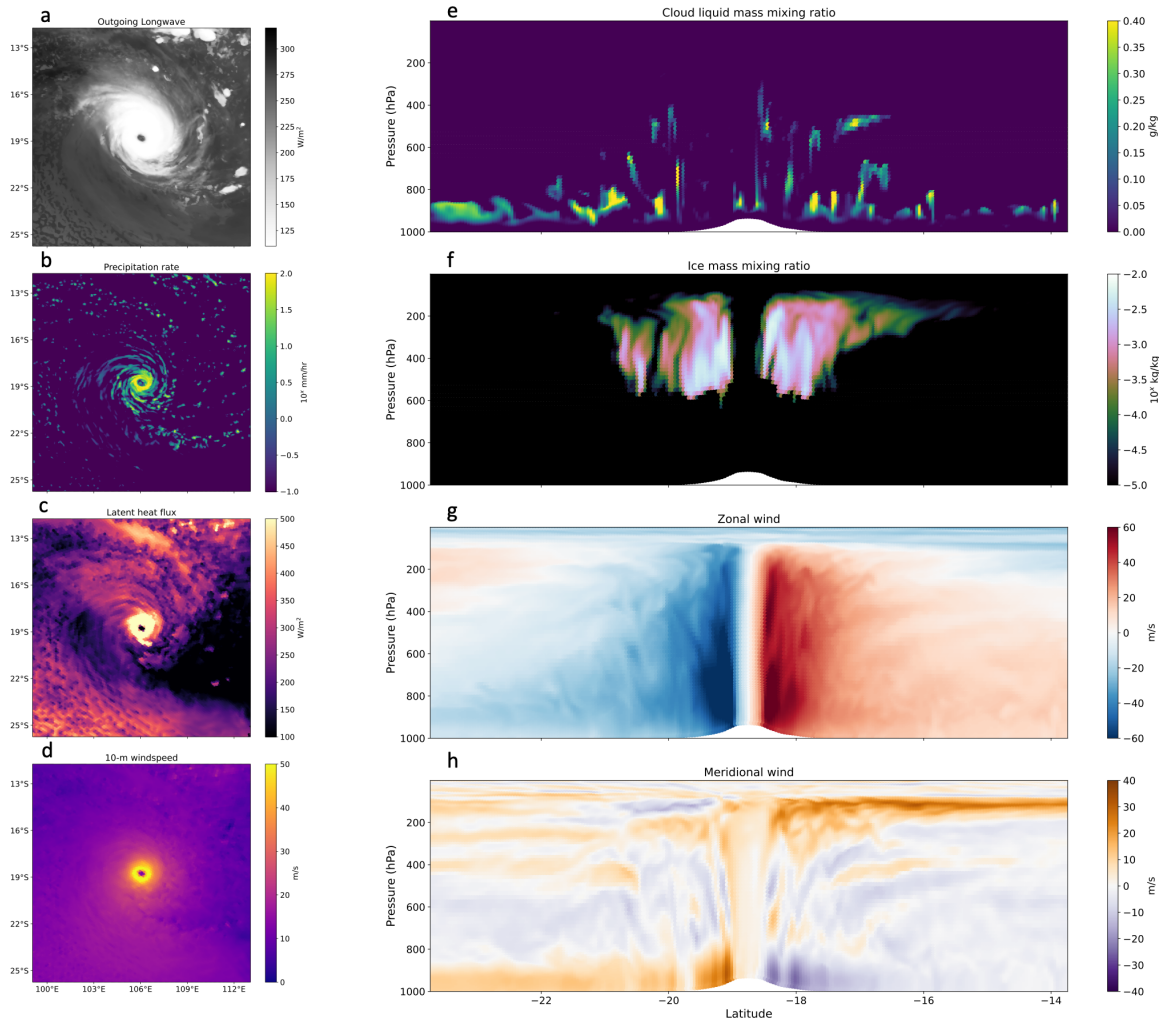


**Figure 20.** Instantaneous planar and curtain view of Feb 11 tropical cyclone at maximum intensity on Feb 16 00UTC. On the left column are planar views of the outgoing longwave radiation (a), precipitation rate (b), latent heat flux (c), and 10-m wind speed (d). On the right column is a north-south curtain snapshot through the center of the storm of the cloud liquid mass mixing ratio (e), ice mass mixing ratio (f), zonal wind speed (g), and meridional wind speed (h).

792 MOND. However, as Fig. 19 and 20 indicate, SCREAM produces tropical cyclones with  
 793 reasonable eye-wall structure and adequate surface wind intensities, which provide promise for  
 794 future attempts to simulate observed tropical cyclones using the model.

## 795 6.6 Extratropical Cyclones

796 In mid- and high-latitude regions, extratropical cyclones (ECs) are a large source  
 797 of day-to-day weather variability. ECs are a major pathway for water evaporated from  
 798 the ocean to precipitate over land; Hawcroft et al. (2012) suggest that as much as 90%  
 799 of the surface precipitation along midlatitude storm tracks is attributed to ECs. ECs are  
 800 also behind a majority of extreme precipitation events, particularly in the northeast US  
 801 where ECs are responsible for more than 80% of winter-time extreme precipitation (Pfahl  
 802 & Wernli, 2012; Agel et al., 2015). With increasing resolution, ECs are better represented

803 in global models (Jung et al., 2006), and a recent study using a set of global storm-resolving  
 804 model simulations shows an increase of 7%/K in precipitation rate from the most intense  
 805 extratropical cyclones with warming, which differs from the 2-3%/K increase expected  
 806 in the global mean (Kodama et al., 2019).

807 Over the simulation time period, 87 ECs are identified in SCREAM and 80 are found  
 808 in ERA5 using the TempestExtremes algorithm (see Appendix A2 for details). Their ge-  
 809 ographic distributions in the Southern and Northern Hemispheres are shown in Fig. 21a  
 810 and b. In the Northern Hemisphere, the density of storms in both SCREAM and ERA5  
 811 is largest over the Atlantic and Pacific Ocean basins, with many storms originating close  
 812 to the western boundary currents. This is consistent with observed climatologies of cy-  
 813 clone statistics (Sinclair, 1997). Bomb cyclones (ECs with surface low pressures drop-  
 814 ping more than 24 hPa over a 24 hour period (Sanders & Gyakum, 1980)) are present  
 815 in both SCREAM (11) and in ERA5 (15). While small numbers prevent us from mak-  
 816 ing conclusive statements, spatial distributions in ERA5 and SCREAM seem consistent.

817 Fig. 21c shows the frequency of ECs by latitude band. ECs are counted separately  
 818 in each 6 hourly snapshot in this plot, so counts in this plot are much higher than the  
 819  $\sim 80$  storms quoted above for SCREAM and ERA5, which tracked single storms across  
 820 time. In both hemispheres, SCREAM has a more peaked distribution with maximum  
 821 frequency at the upper limit of the observed count from the 1979-2020 period. The ex-  
 822 cessively peaked EC count structure in the northern hemisphere is consistent with zonal  
 823 precipitation bias shown in Fig. 13. Interestingly, modeled southern hemisphere storm  
 824 track precipitation in Fig. 13 matches ERA5 almost perfectly despite having excessive  
 825 EC count around 50°S. Storm composites show that Southern Hemisphere extratrop-  
 826 ical cyclones in SCREAM are associated with less rain than ERA5, which might explain  
 827 this apparent paradox (not shown). Peak latitude is roughly consistent with observations  
 828 in each hemisphere, though is displaced slightly poleward in the northern hemisphere.

829 We noted earlier that large swaths of the Southern Ocean in SCREAM have too  
 830 much absorbed shortwave radiation compared to CERES-EBAF retrievals (Fig. 9). Many  
 831 climate models share biases where the cold sector of storms does not reflect enough in-  
 832 coming shortwave radiation, while the warm sector is less biased (Bodas-Salcedo et al.,  
 833 2014). To examine whether this is the case in SCREAM, we construct composites of the  
 834 cyclones tracked in SCREAM between 40°S and 60°S. This latitude band is consistent  
 835 with those of Bodas-Salcedo et al. (2014), but ignores storms with centers poleward of  
 836 60°S (to remove complications due to the reflectivity of sea ice). Fig. 22 shows the com-  
 837 posite of the pseudo-cloud albedo for SCREAM and its difference with CERES-SYN-  
 838 based estimates. The pseudo-cloud albedo is defined here as the shortwave cloud radi-  
 839 ative effect divided by the local solar insolation. By using a pseudo-cloud albedo rather  
 840 than reflected shortwave radiation, we remove the potential impact of biases in the lat-  
 841 itudinal distribution of ECs on our assessment of SCREAM’s cloud reflectivity. Indeed,  
 842 like the GCMs studied by Bodas-Salcedo et al. (2014), there is less cloud reflection in  
 843 the cold sector of SCREAM’s storms (-4.9 % in the cold western half of the storm), com-  
 844 pared to the storms captured in ERA5. However, the warm-sector of the storm also shows  
 845 lower cloud albedo (-3.8 % in the warm eastern half of the storm), showing that in SCREAM,  
 846 there is a general lack of cloud reflection. Fixing this bias is a research priority.

## 847 6.7 Atmospheric Rivers

848 Atmospheric rivers (ARs) are long, narrow, and transient corridors of enhanced va-  
 849 por transport typically associated with the low-level jet stream ahead of the cold front  
 850 of an extratropical cyclone (AMS, 2019). As noted by Zhu and Newell (1998), ARs are  
 851 responsible for approximately 90% of poleward vapor transport. Water resources in the  
 852 western U.S. are strongly tied to ARs, with landfalling ARs providing approximately 20–  
 853 50% of total wet season precipitation (Dettinger et al., 2011; Lavers & Villarini, 2015)

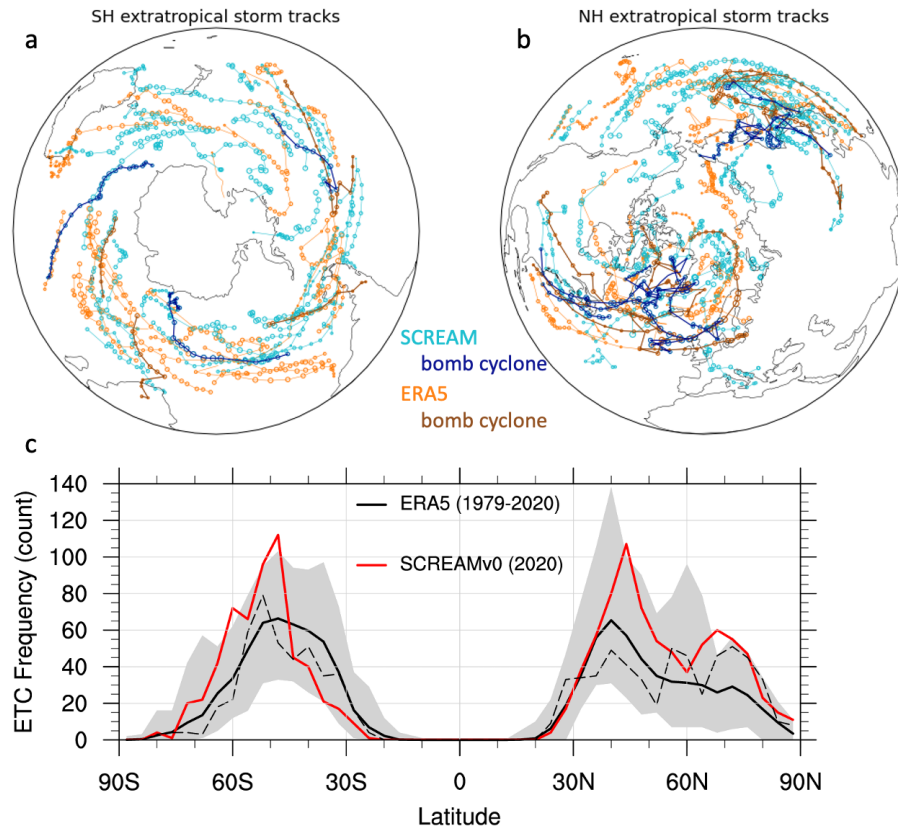


**Figure 21.** Geographic distribution of extratropical cyclones identified in SCREAM (cyan) and ERA5 (orange) using the TE algorithm (described in Appendix A2) for the Southern Hemisphere (a) and Northern Hemisphere (b). Dark blue tracks indicate bomb cyclones in SCREAM, whereas brown tracks indicate bomb cyclones in ERA5. (c) The latitudinal distribution of 6 hourly snapshots of extratropical cyclones in ERA5 (black) and SCREAM (red). The dashed black line indicates the distribution found in ERA5 for the DYAMOND2 period (Jan 20 through Feb 28, 2020). Solid black line indicates the average distribution for Jan 20 to Feb 28 of 1979 through 2020 in ERA5 with gray shading indicating maximum and minimum ranges for each year.

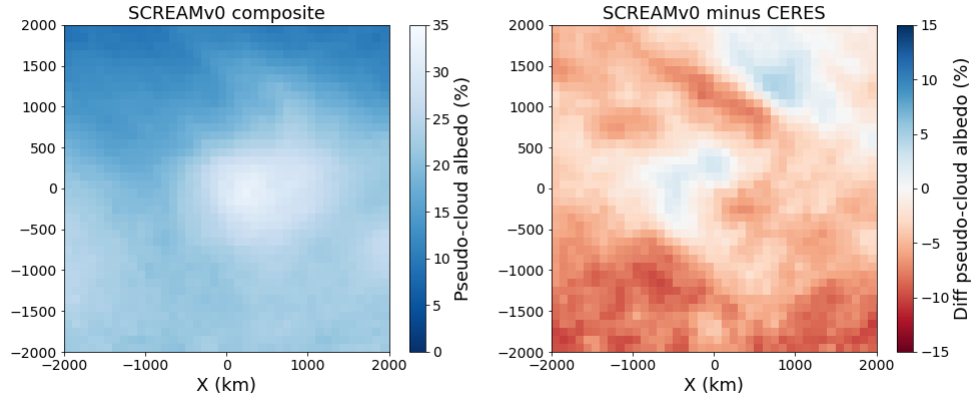


**Figure 22.** (left) Composite of the pseudo-cloud albedo in extratropical cyclones found between  $45^{\circ}\text{S}$  and  $60^{\circ}\text{S}$  in SCREAM (Jan 20 – Feb 28). Composites average over all 6 hourly snapshots centered on identified ECs and are plotted such that north is oriented upward. (right) Difference in storm composite pseudo-cloud albedo between storms in SCREAM and in reanalysis and satellite data (ERA5 / CERES-SYN) for storms occurring during the same period.

854 and 30 – 40% of mountain snowpack (Guan et al., 2010). One such landfalling atmo-  
 855 spheric river observed in the SCREAM simulation along the west coast of North Amer-  
 856 ica is depicted in Fig. 23.

857 To assess the quality of ARs in the SCREAM simulation, we track ARs over the  
 858 simulation period using the TempestExtremes atmospheric river detection and tracking  
 859 algorithm (McClenny et al., 2020; Ullrich & Zarzycki, 2017) as described in Appendix  
 860 A3. In Fig. 24 the properties of these tracked features are then compared to analogously  
 861 tracked features from all January 20 through Mar 28 periods in ERA5 data (1979-2020),  
 862 roughly following the approach discussed in Rutz et al. (2019). In general SCREAM falls  
 863 well within the climatological range from ERA5 historical simulations, except for a slight  
 864 underestimation of AR frequency around  $35^{\circ}$  north and south of  $50^{\circ}\text{S}$ . For 2020, ERA5  
 865 predicts abnormally high AR activity while SCREAM is slightly weaker than ERA5’s  
 866 long-term average. Without an ensemble of simulations to compare against, however, such  
 867 a discrepancy could very easily be attributed to interannual variability.

868 The underestimation of AR frequency in southern high latitudes is associated with  
 869 anomalously low eastward integrated vapor transport (IVT), which is in turn due to anoma-  
 870 lously low eastward wind speeds compared to ERA5 (not shown). Interestingly, Fig. 21  
 871 shows that EC frequency was actually *too high* where we find AR frequency to be too  
 872 low. Perhaps ECs are spending too much time in this region due to low wind speeds?  
 873 Nonetheless, the fractional contribution of ARs to poleward transport of moisture is al-  
 874 most identical to the climatological mean performance from ERA5, suggesting consis-  
 875 tency of the underlying physical processes. Overall we conclude that SCREAM performs  
 876 well in its representation of ARs and their associated contribution to poleward transport  
 877 of vapor.

## 878 6.8 Cold-Air Outbreaks

879 Marine cold air outbreaks (MCAOs) occur when cold air of polar or continental  
 880 origin flow over warm ocean waters. Because of the strong air-sea temperature differ-  
 881 ences and typical higher surface wind speeds, cold air outbreaks are regions of strong sur-  
 882 face turbulent heat fluxes that can reach  $1000 \text{ W m}^{-2}$  (Shapiro et al., 1987) and can im-

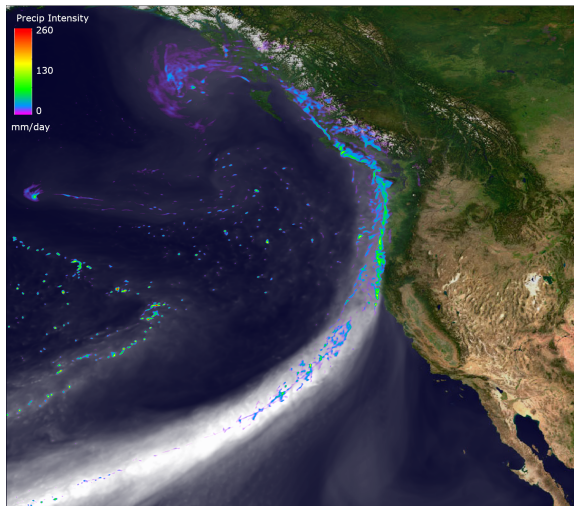


**Figure 23.** Snapshot of a landfalling atmospheric river along the west coast of North America that occurs on February 11th 23:00:00 UTC. Vertically-integrated water vapor is indicated in transparent grayscale with opaque/white regions having integrated vapor greater than  $40 \text{ kg m}^{-2}$ . Colors indicate precipitation intensity.

883 pact frontogenesis (Terpstra et al., 2016). General circulation models (GCMs) have, how-  
 884 ever, not represented clouds under these conditions very well (Rémillard & Tselioudis,  
 885 2015). The models tend to simulate too little stratiform cloud cover in these regions (Field  
 886 et al., 2014; Bodas-Salcedo et al., 2014). In this section, we describe the frequency and  
 887 intensity of MCAOs in the SCREAM simulation relative to reanalysis (ERA5) during  
 888 the same time period and examine the surface flux and cloud properties for a single cold  
 889 air outbreak event that occurs early in the simulation over the Kuroshio current.

890 To identify and quantify cold air outbreaks, we use the cold air outbreak index ( $M$ )  
 891 as described by Fletcher et al. (2016), which is quantified as the potential temperature  
 892 difference between the surface skin and 800hPa. Any oceanic region with a positive value  
 893 of  $M$  denotes a region undergoing a cold air outbreak. If we compare the frequency of  
 894 cold air outbreaks in SCREAM and in ERA5 over the global oceans, we see general agree-  
 895 ment of where and how often cold air outbreaks occur (Fig. 25a and c). Cold air out-  
 896 breaks tend to occur most prominently in the winter Northern Hemisphere along the east-  
 897 ern edges of continents and southern edges of the sea-ice. In regions where SCREAM  
 898 produces cold air outbreaks (e.g. over the Kuroshio current, Gulf stream current, and  
 899 south of Alaska),  $M$  frequency tends to be higher. MCAOs are, however, greatly under-  
 900 estimated to the south and east of Greenland. This is unsurprising since 2-m temper-  
 901 ature is far too warm over Greenland (Fig. 6), likely due to meridional wind biases dis-  
 902 cussed in Sect. 6.2. Except for a slight overestimation, SCREAM also tends to capture  
 903 well the intensity of the strongest of cold air outbreaks (Fig. 25b and d).

904 To study the cloud fields that form under the simulated cold air outbreaks in SCREAM,  
 905 we focus on a cold air outbreak event that flows off the Asian continent over the Kuroshio  
 906 current from Jan 21st to Jan 22nd. We examine the cold air outbreak characteristics over  
 907 the 24 hour period of Jan 22nd to exclude any impacts of the cold front. The simulated  
 908 sensible heat flux generally matches ERA5, but is a bit too smooth and too big (Fig. 26a  
 909 and d). Good spatial agreement may be an artifact of prescribed SST; smooth features  
 910 are probably due to use of a coarser ( $\sim 6 \text{ km}$ ) ocean grid in this region. Excessive mag-  
 911 nitude is unsurprising given surface wind speed biases mentioned in Sect. 6.2 and again

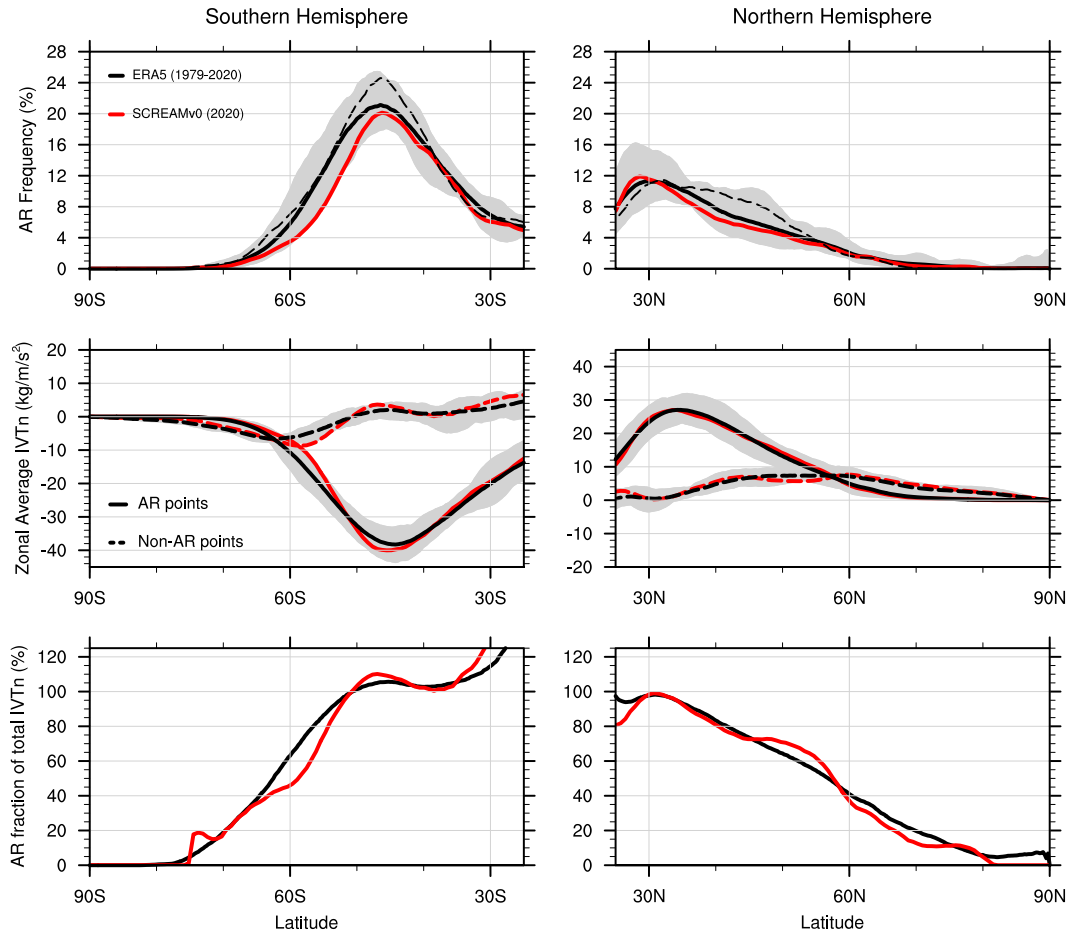


**Figure 24.** Properties of tracked atmospheric rivers in both hemispheres over the period January 20 through February 28 of each year in (red) the SCREAM DYAMOND2 simulation and (gray shaded region with mean shown with black solid line) 1979-2020 ERA5 reanalysis. Plots refer to (top) average atmospheric river frequency, as a percent of the full longitudinal band, with results from 2020 depicted with a black dashed line; (middle) zonally averaged northward integrated vapor transport (IVTn) at grid points flagged as part of / not part of atmospheric rivers; (bottom) mean fractional contribution of northward vapor transport from atmospheric rivers relative to all northward vapor transport.

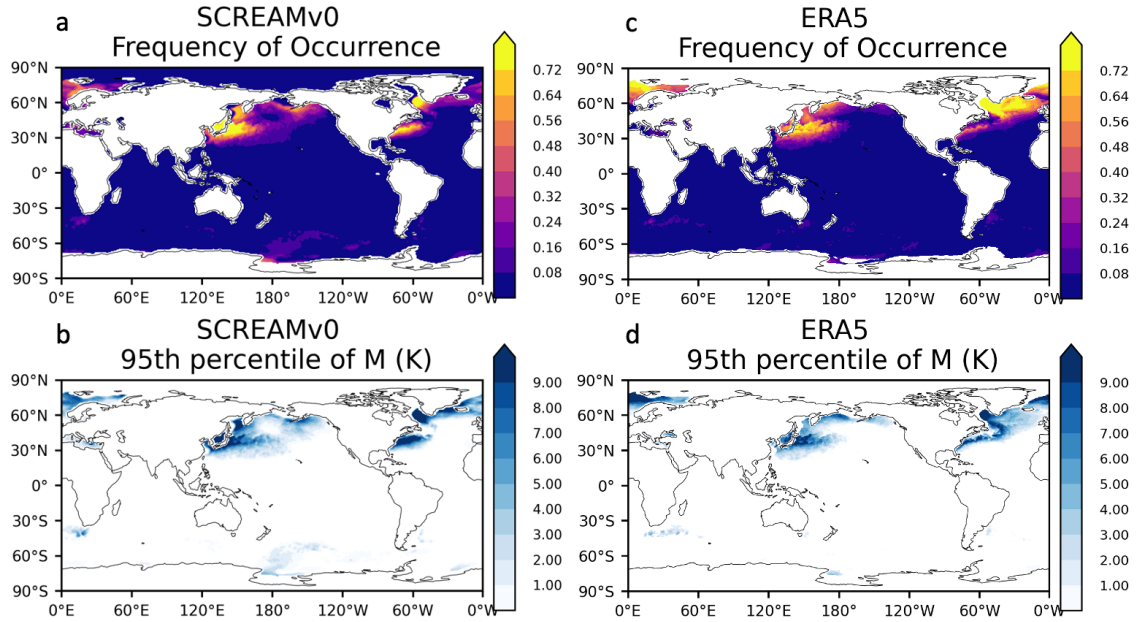


**Figure 25.** Frequency of cold air outbreaks (based on the  $M$  of Fletcher et al., 2016) in SCREAM over the month of February 2020 in SCREAM (a) and in ERA5 (c). Also shown is the 95th percentile value of  $M$  (including non-cold air outbreak instances) over the same period in SCREAM (b) and ERA5 (d).

912 apparent from comparing Fig. 26 panels b versus e. Surface air temperature bias does  
 913 not contribute to excessive surface fluxes (not shown).

914 Although GCMs tend to underestimate the occurrence of MCAO clouds and SCREAM  
 915 itself was shown earlier to suffer from a deficiency in clouds in other regimes, a compar-  
 916 ison of the shortwave cloud radiative effect between the model and CERES-SYN sug-  
 917 gests good agreement in the MCAO regime (Fig. 26c and f). In Fig. 27 we take a closer  
 918 look at cloud structure by comparing a snapshot of shortwave cloud radiative effect from  
 919 SCREAM against a visible satellite image taken at the same time from Himawari-8 (Bessho  
 920 et al., 2016). Similarity between the observed and simulated cloud structures is strik-  
 921 ing, particularly since this image is taken 2 days into a free-running simulation. In par-  
 922 ticular, cloud streets in SCREAM form along the direction of the flow, before transition-  
 923 ing into broken and open-cellular convection further offshore. The model’s ability to cap-  
 924 ture this transition suggests that SCREAM’s combination of resolution and boundary  
 925 layer/cloud parameterizations contains the physics necessary to capture cloud transitions  
 926 in cold air outbreaks. Further analyses compositing many cold air outbreak events would  
 927 be necessary to draw more general conclusions.

## 928 7 Conclusions

929 The overall takeaway from this work is that 3.25 km global models solve a lot of  
 930 the long-standing problems in global climate modeling even without the detailed opti-  
 931 mization and tuning which is typically so important for GCM skill. In particular, SCREAM  
 932 does an excellent job simulating precipitation; its diurnal cycle (Fig. 15) and intensity  
 933 distribution (Fig. 16) are particularly realistic. Tropical and extratropical storm frequency  
 934 and structure (Sections 6.5-6.7) are also impressive. The vertical structure of tropical  
 935 convection (Fig. 10) is also much improved relative to typical GCMs. Coastal stratocu-

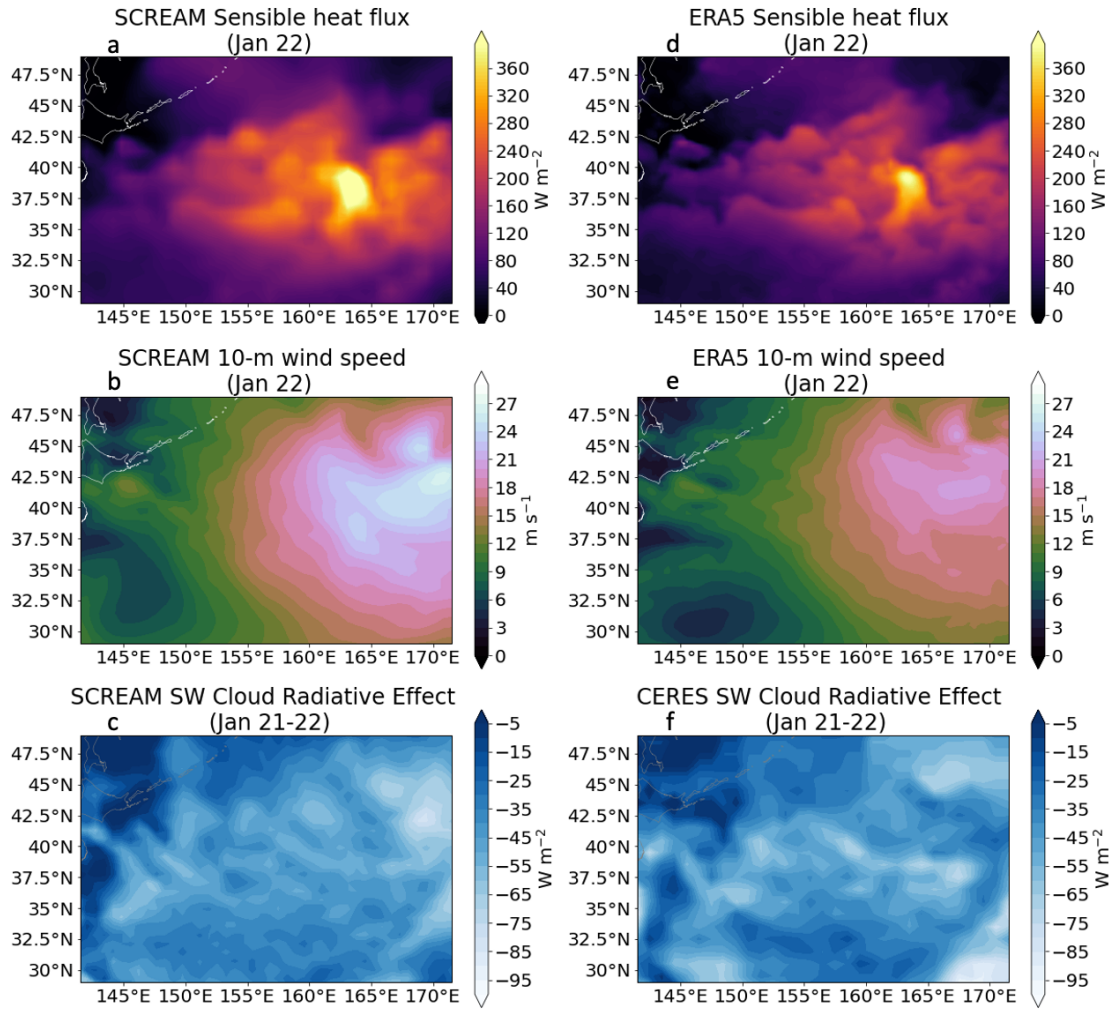


**Figure 26.** The daily-mean sensible heat flux over the Kuroshio region bounded from 29N to 49N and 141.5E to 171.5E in SCREAM (a) and ERA5 (d) for the cold air outbreak on January 22. Also shown are similar daily mean values of 10-m wind speed (b - SCREAM; e - ERA5) and shortwave cloud radiative effect (c - SCREAM; f - CERES-SYN).

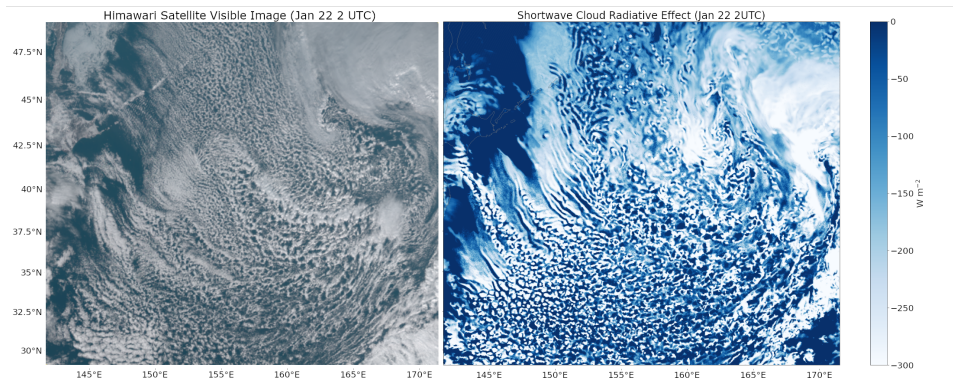


**Figure 27.** Cold-air outbreak off Siberia on January 22nd 2020 at 2:00:00 UTC ( $\sim$ local noon) from a Himawari visible satellite image (left) and shortwave cloud radiative effect from SCREAM (right). Visualization is over a region bounded by 29N to 49N and 141.5E to 171.5E.

936 mulus (Fig. 11) and cold-air outbreaks (25-27), which are perennially difficult to sim-  
 937 ulate not just in GCMs (Rémillard & Tselioudis, 2015) but also in limited-area CPMs  
 938 (Klein et al., 2009), are also well captured. We suspect that the SHOC cloud/turbulence  
 939 parameterization and fine vertical resolution within SCREAM were important for this  
 940 success.

941 Several biases in SCREAM are familiar from conventional GCMs. Clarifying whether  
 942 these biases are caused by processes unresolved at 3.25 km grid spacing would be a large  
 943 step towards understanding and therefore fixing these perennial problems. One such bias  
 944 is the tendency for the South Pacific Convergence Zone to be too zonal (Fig. 13-14). This  
 945 suggests that resolution doesn't resolve the double-ITCZ bias that plagues lower-resolution  
 946 models. This finding is consistent with the result of Stevens et al. (2019) for other GCPMs.  
 947 Another bias in lower-resolution versions of E3SM which persists in SCREAM is a ten-  
 948 dency for precipitation in the West Pacific to be maximized over the Maritime Conti-  
 949 nent rather than to the east over the ocean.

950 Analysis for this paper also revealed several deficiencies which will be fixed in fu-  
 951 ture model versions. First, cloud fraction near the tropopause is corrupted by the use  
 952 of a relative-humidity based ice cloud fraction scheme tuned for low resolutions (Fig. 4).  
 953 Because these spurious clouds had no mass, they had little practical impact on the sim-  
 954 ulation, but users of SCREAM DYAMOND2 data should be careful to use our post-facto-  
 955 generated cloud-mask-based cloud fraction for future analysis. Overly strong surface wind  
 956 speed is a second deficiency (Fig. 7). Upper level winds are generally reasonable but have  
 957 unrealistic poleward transport south of Greenland and around Australia (Fig. 8). Sur-  
 958 face temperature at high latitudes is also problematic (Fig. 6). One potential reason for  
 959 this is a land initial condition with low snowpack in mountainous regions exacerbated  
 960 by potentially poor tuning of the lower limit on turbulent mixing in stable conditions  
 961 and aforementioned biases related to heat transport into polar regions. Another issue  
 962 is a prevalence of frequent, small "popcorn" convective events (Fig. 17). Finally, cloud  
 963 tuning should be improved. Shortwave reflection and longwave emission are too weak  
 964 (Fig. 9) and low-level clouds tend too much towards stratus and too little towards shal-  
 965 low convection (Fig. 12). Issues like these are expected for a new model version and many  
 966 of these issues have an obvious solution. We are releasing this initial model without fix-  
 967 ing these problems to match the timing of the DYAMOND2 intercomparison, because  
 968 there will *always* be something else to fix, and because using a model for science and writ-  
 969 ing papers is by far the fastest way to find problems.

970 This simulation is a milestone rather than an endpoint in SCREAM development.  
 971 In addition to fixing the issues identified above, the major focus of the SCREAM project  
 972 is on completing the computationally-performant C++ implementation of the model.  
 973 We hope to perform longer, more realistic simulations soon.

## 974 **Appendix A Feature tracking with TempestExtremes**

975 For feature tracking in the DYAMOND2 simulation we use TempestExtremes 2.1  
 976 (Ullrich & Zarzycki, 2017), available from ZENODO at <http://dx.doi.org/10.5281/zenodo.4385656> and GitHub at <https://github.com/ClimateGlobalChange/tempestextremes>.  
 977 The exact commands employed in this analysis are provided in this section for reference.  
 978

### 979 **A1 Tropical Cyclones**

980 Tropical cyclone tracking is performed on 6-hourly data following (Zarzycki et al.,  
 981 2017). The search is performed for local minima in the sea level pressure (PSL) which  
 982 are accompanied by an increase of 200 Pa over a distance of 5.5 degrees great circle dis-  
 983 tance (GCD). Tropical cyclones are further defined by the presence of an upper-level warm  
 984 core which is characterized by anomalous thickness in the geopotential height between

985 500 hPa and 200 hPa. Here we require that this thickness drop by 6.0 meters over a dis-  
 986 tance of 6.5 degrees GCD, where the maxima in the layer thickness must be within 1.0  
 987 degrees GCD of the pressure minima. Following this only the most intense features within  
 988 6.0 degrees GCD are retained. Tracks are then stitched together in time, where sequen-  
 989 tial features must be within 8.0 degrees GCD, must persist for at least 10 time steps (2.5  
 990 days), can have no more than 3 sequential 6-hourly time steps where no detection is found,  
 991 must have a 10 meter wind speed greater than  $10 \text{ m s}^{-1}$  for at least 10 steps along the  
 992 trajectory, and must be within  $50^\circ\text{S}$  and  $50^\circ\text{N}$  for at least 10 steps along the trajectory.  
 993 The commands are as follows:

```
994 $STEMPESTEXTREMESDIR/DetectNodes --in_data_list DYAMOND_TC_files.txt
995 --out DYAMOND_DN.txt --searchbymin PSL
996 --closedcontourcmd "PSL,200.0,5.5,0;_DIFF(Z200,Z500),-6.0,6.5,1.0"
997 --mergedist 6.0 --outputcmd "PSL,min,0;WINDSPD_10M,max,2" --timefilter "6hr"
998
999 $STEMPESTEXTREMESDIR/StitchNodes --in DYAMOND_DN.txt
1000 --out DYAMOND_TC_tracks.txt --in_fmt "lon,lat,slp,wind" --range 8.0
1001 --mintime "10" --maxgap "3"
1002 --threshold "wind,>=,10.0,10;lat,<=,50.0,10;lat,>=,-50.0,10"
```

## 1003 A2 Extratropical Cyclones

1004 As with tropical cyclones, extratropical cyclone tracking is performed on 6-hourly  
 1005 data. Candidates are first detected as minima in the difference between the sea-level pres-  
 1006 sure (PSL) and the average sea-level pressure over the entire simulation (PSL\_climo).  
 1007 We require that this difference increase by 200 Pa within 5.5 degrees GCD of the can-  
 1008 didate. We further eliminate points that have an upper-level warm core, as these are likely  
 1009 tropical cyclones, by removing candidates with a drop in the 500-200hPa layer thickness  
 1010 of 6.0 meters within 6.5 degrees GCD of the point of maximum layer thickness within  
 1011 1.0 degrees of the candidate. Following this only the most intense features within 6.0 de-  
 1012 grees GCD are retained. Tracks are then stitched together in time, where sequential fea-  
 1013 tures must be within 8.0 degrees GCD, must persist for at least 8 time steps (2.0 days),  
 1014 can have no more than 2 sequential 6-hourly time steps where no detection is found, must  
 1015 have a surface geopotential less than 700.0 for at least 8 time steps, and must have a dis-  
 1016 tance of 6.0 degrees GCD between genesis and termination point. The commands for these  
 1017 operations are as follows:

```
1018 $STEMPESTEXTREMESDIR/bin/DetectNodes --in_data_list DYAMOND_ETC_files.txt
1019 --out DYAMOND_DN_ETCs.txt --searchbymin "_DIFF(PSL,PSL_climo)" --timefilter "6hr"
1020 --closedcontourcmd "_DIFF(PSL,PSL_climo),200.0,5.5,0"
1021 --noclosedcontourcmd "_DIFF(Z200,Z500),-6.0,6.5,1.0" --mergedist 6.0
1022 --outputcmd "PSL,min,0;_DIFF(PSL,PSL_climo),min,0;WINDSPD_10M,max,5;PHIS,min,0"
1023
1024 $STEMPESTEXTREMESDIR/bin/StitchNodes --in DYAMOND_DN_ETCs.txt
1025 --out DYAMOND_ETC_tracks.txt --in_fmt "lon,lat,psl,pslanom,wind,phis" --range 8.0
1026 --mintime "8" --maxgap "2" --min_endpoint_dist 6.0 --threshold "phis,<=,700,8"
```

## 1027 A3 Atmospheric Rivers

1028 Atmospheric river tracking is performed using the tracker employed in (McClenny  
 1029 et al., 2020). Grid points poleward of 15 degrees N/S are flagged where the Laplacian  
 1030 of the integrated vapor transport (evaluated using 8 points with radius 10 degrees GCD)  
 1031 is less than  $20000 \text{ kg m}^{-1} \text{ s}^{-1} \text{ rad}^{-2}$ . Only contiguous regions with area greater than  
 1032  $4 \times 10^5 \text{ km}^2$  are retained in this operation. Since high IVT blobs can include tropical

1033 cyclones, we also remove all points within 10 degrees GCD of TCs detected using the  
1034 method described in section A1. The commands for these operations are as follows:

```
1035 $STEMPESTEXTREMESDIR/DetectBlobs --in_data CAT_TUQ,TVQ_256x512.eam.nc
1036 --out CAT_ARs_256x512.eam.nc --minabslat 15 --geofiltercmd "area,>=,4e5km2"
1037 --thresholdcmd "_LAPLACIAN{8,10}(_VECMAG(TUQ,TVQ)),<=,-20000,0"
1038
1039 $STEMPESTEXTREMESDIR/NodeFileFilter --in_nodefile DYAMOND_TC_tracks.txt
1040 --in_fmt "lon,lat" --in_data CAT_ARTag_256x512.eam.nc
1041 --out_data CAT_ARTag_TCfiltered_256x512.eam.nc --var "binary_tag"
1042 --bydist 10.0 --invert
```

## 1043 Acknowledgments

1044 This research was supported as part of the Energy Exascale Earth System Model  
1045 (E3SM) project, funded by the U.S. Department of Energy, Office of Science, Office of  
1046 Biological and Environmental Research. It used resources of the National Energy Re-  
1047 search Scientific Computing Center (NERSC), a U.S. Department of Energy Office of  
1048 Science User Facility located at Lawrence Berkeley National Laboratory, operated un-  
1049 der Contract No. DE-AC02-05CH11231. This research also used resources from the Ar-  
1050 gonne Leadership Computing Facility at Argonne National Laboratory, which is supported  
1051 by the Office of Science of the U.S. Department of Energy under contract DE-AC02-06CH11357.  
1052 This paper was prepared by LLNL under Contract DE-AC52-07NA27344. H.-Y. Ma is  
1053 funded by the Regional and Global Model Analysis program area and Atmospheric Sys-  
1054 tem Research program of the U.S. Department of Energy. Sandia National Laborato-  
1055 ries is a multimission laboratory managed and operated by National Technology and En-  
1056 gineering Solutions of Sandia, LLC, a wholly owned subsidiary of Honeywell International  
1057 Inc., for the U.S. Department of Energy's National Nuclear Security Administration un-  
1058 der contract DE-NA0003525. This paper describes objective technical results and anal-  
1059 ysis. Any subjective views or opinions that might be expressed in the paper do not nec-  
1060 essarily represent the views of the U.S. Department of Energy or the United States Gov-  
1061 ernment. The SCREAM output described in this paper is publicly available as part of  
1062 the DYAMOND2 intercomparison as described at [https://www.esiwace.eu/services/](https://www.esiwace.eu/services/diamond)  
1063 [diamond](https://www.esiwace.eu/services/diamond). The GPM dataset used in this study is Version 06B Level 3 half-hourly 0.1 de-  
1064 gree x 0.1 degree final-run gauge-calibrated data as described in G. Huffman et al. (2019)  
1065 and accessible via [https://disc.gsfc.nasa.gov/datasets/GPM\\_3IMERGHH.06/summary](https://disc.gsfc.nasa.gov/datasets/GPM_3IMERGHH.06/summary).  
1066 We acknowledge and thank Jingyu Wang for accessing, formatting, and making the data  
1067 available to us. The version of CERES SYN1deg data used here is Edition 4.1 with a  
1068 release date of August 22, 2019 and was accessed from: [https://ceres-tool.larc.nasa](https://ceres-tool.larc.nasa.gov/ord-tool/jsp/SYN1degEd41Selection.jsp)  
1069 [.gov/ord-tool/jsp/SYN1degEd41Selection.jsp](https://ceres-tool.larc.nasa.gov/ord-tool/jsp/SYN1degEd41Selection.jsp). The Himawari-8 visible image used  
1070 in this paper was supplied by the P-Tree System of the Japan Aerospace Exploration  
1071 Agency (JAXA). The authors would also like to thank Jiwen Fan and Kai Zhang for their  
1072 contributions to fixing bugs in our P3 microphysics implementation and 3 anonymous  
1073 reviewers for excellent suggestions to improve the manuscript.

## 1074 References

- 1075 Abdul-Razzak, H., & Ghan, S. J. (2000). A parameterization of aerosol activa-  
1076 tion: 2. multiple aerosol types. *Journal of Geophysical Research: Atmospheres*,  
1077 *105*(D5), 6837-6844. doi: <https://doi.org/10.1029/1999JD901161>
- 1078 Agel, L., Barlow, M., Qian, J.-H., Colby, F., Douglas, E., & Eichler, T. (2015).  
1079 Climatology of Daily Precipitation and Extreme Precipitation Events in the  
1080 Northeast United States. *Journal of Hydrometeorology*, *16*(6), 2537-2557. doi:  
1081 [10.1175/JHM-D-14-0147.1](https://doi.org/10.1175/JHM-D-14-0147.1)

- 1082 AMS. (2019, March). *Atmospheric river*. American Meteorological Society. Re-  
 1083 trieved from [http://glossary.ametsoc.org/wiki/Atmospheric\\_river](http://glossary.ametsoc.org/wiki/Atmospheric_river)
- 1084 Arnold, N. P., Putman, W. M., & Freitas, S. R. (2020). Impact of Resolution and  
 1085 Parameterized Convection on the Diurnal Cycle of Precipitation in a Global  
 1086 Nonhydrostatic Model. *Journal of the Meteorological Society of Japan. Ser. II,*  
 1087 *advpub*. doi: 10.2151/jmsj.2020-066
- 1088 Ascher, U. M., Ruuth, S. J., & Spiteri, R. J. (1997). Implicit-explicit Runge-Kutta  
 1089 methods for time-dependent partial differential equations. *Applied Num.*  
 1090 *Math.*, 25(2-3), 151–167. doi: 10.1016/s0168-9274(97)00056-1
- 1091 Atlas, R., Reale, O., Shen, B.-W., Lin, S.-J., Chern, J.-D., Putman, W., ...  
 1092 Radakovich, J. (2005). Hurricane forecasting with the high-resolution nasa  
 1093 finite volume general circulation model. *Geophysical Research Letters*, 32(3).  
 1094 doi: 10.1029/2004GL021513
- 1095 Austin, R. T., Heymsfield, A. J., & Stephens, G. L. (2009). Retrieval of ice cloud  
 1096 microphysical parameters using the cloudsat millimeter-wave radar and tem-  
 1097 perature. *Journal of Geophysical Research: Atmospheres*, 114(D8). doi:  
 1098 <https://doi.org/10.1029/2008JD010049>
- 1099 Bacmeister, J. T., Wehner, M. F., Neale, R. B., Gettelman, A., Hannay, C., Lau-  
 1100 ritzen, P. H., ... Truesdale, J. E. (2014). Exploratory high-resolution climate  
 1101 simulations using the community atmosphere model (cam). *Journal of Cli-*  
 1102 *mate*, 27(9), 3073-3099. doi: 10.1175/JCLI-D-13-00387.1
- 1103 Bergeron, T. (1935). *On the physics of clouds and precipitation*. Proces Verbaux  
 1104 de l'Association de Météorologie, International Union of Geodesy and Geo-  
 1105 physics.
- 1106 Bertagna, L., Deakin, M., Guba, O., Sunderland, D., Bradley, A. M., Tezaur, I. K.,  
 1107 ... Salinger, A. G. (2019). Hommexx 1.0: a performance-portable atmospheric  
 1108 dynamical core for the energy exascale earth system model. *Geoscientific*  
 1109 *Model Development*, 12(4), 1423–1441. doi: 10.5194/gmd-12-1423-2019
- 1110 Bertagna, L., Guba, O., Taylor, M., Foucar, J., Larkin, J., Bradley, A., ... Salinger,  
 1111 A. (2020). A performance-portable nonhydrostatic atmospheric dycore for the  
 1112 energy exascale earth system model running at cloud-resolving resolutions. In  
 1113 *2020 SC20: International Conference for High Performance Computing, Net-*  
 1114 *working, Storage and Analysis (SC)* (p. 1304-1317). Los Alamitos, CA, USA:  
 1115 IEEE Computer Society. doi: 10.1109/SC41405.2020.00096
- 1116 Bessho, K., Date, K., Hayashi, M., Ikeda, A., Imai, T., Inoue, H., ... Yoshida, R.  
 1117 (2016). An introduction to himawari-8/9; japan's new-generation geostationary  
 1118 meteorological satellites. *Journal of the Meteorological Society of Japan. Ser.*  
 1119 *II*, 94(2), 151-183. doi: 10.2151/jmsj.2016-009
- 1120 Bodas-Salcedo, A., Williams, K. D., Ringer, M. A., Beau, I., Cole, J. N. S.,  
 1121 Dufresne, J.-L., ... Yokohata, T. (2014). Origins of the Solar Radiation  
 1122 Biases over the Southern Ocean in CFMIP2 Models. *Journal of Climate*,  
 1123 27(1), 41–56. doi: 10.1175/JCLI-D-13-00169.1
- 1124 Bogenschutz, P., & Krueger, S. K. (2013). A simplified PDF parameteri-  
 1125 zation of subgrid-scale clouds and turbulence for cloud-resolving mod-  
 1126 els. *Journal of Advances in Modeling Earth Systems*, 5(2), 195-211. doi:  
 1127 <https://doi.org/10.1002/jame.20018>
- 1128 Bogenschutz, P., Yamaguchi, T., & Lee, H.-H. (2021). *E3SM Simulations with high*  
 1129 *vertical resolution in the lower troposphere*. (Accepted, J. Adv. Modeling Earth  
 1130 Sys.)
- 1131 Boyle, J., & Klein, S. A. (2010). Impact of horizontal resolution on climate  
 1132 model forecasts of tropical precipitation and diabatic heating for the twp-  
 1133 ice period. *Journal of Geophysical Research: Atmospheres*, 115(D23). doi:  
 1134 10.1029/2010JD014262
- 1135 Bradley, A. M., Bosler, P. A., Guba, O., Taylor, M. A., & Barnett, G. A. (2019).  
 1136 Communication-efficient property preservation in tracer transport. *SIAM Jour-*

- 1137 *nal on Scientific Computing*, 41(3), C161–C193. doi: 10.1137/18m1165414
- 1138 Bretherton, C. S., & Khairoutdinov, M. F. (2015). Convective self-aggregation feed-  
1139 backs in near-global cloud-resolving simulations of an aquaplanet. *Journal of*  
1140 *Advances in Modeling Earth Systems*, 7(4), 1765–1787. doi: [https://doi.org/10](https://doi.org/10.1002/2015MS000499)  
1141 [.1002/2015MS000499](https://doi.org/10.1002/2015MS000499)
- 1142 Bretherton, C. S., & Park, S. (2009). A new moist turbulence parameterization  
1143 in the community atmosphere model. *Journal of Climate*, 22(12), 3422 - 3448.  
1144 doi: 10.1175/2008JCLI2556.1
- 1145 Caldwell, P. M. (2010). California wintertime precipitation bias in regional and  
1146 global climate models. *Journal of Applied Meteorology and Climatology*,  
1147 49(10), 2147 - 2158. doi: 10.1175/2010JAMC2388.1
- 1148 Caldwell, P. M., Mametjanov, A., Tang, Q., Van Roekel, L. P., Golaz, J.-C., Lin,  
1149 W., ... Zhou, T. (2019). The DOE E3SM Coupled Model Version 1: Descrip-  
1150 tion and Results at High Resolution. *Journal of Advances in Modeling Earth*  
1151 *Systems*, 11(12), 4095–4146. doi: <https://doi.org/10.1029/2019MS001870>
- 1152 Carter-Edwards, H., Trott, C. R., & Sunderland, D. (2014). Kokkos: Enabling  
1153 manycore performance portability through polymorphic memory access pat-  
1154 terns. *J. Parallel and Dist. Comp.*, 74(12), 3202–3216.
- 1155 Cheng, A., & Xu, K.-M. (2008). Simulation of boundary-layer cumulus and stra-  
1156 tocumulus clouds using a cloud-resolving model with low-and third-order  
1157 turbulence closures. *Journal of the Meteorological Society of Japan. Ser. II*,  
1158 86A, 67–86. doi: 10.2151/jmsj.86A.67
- 1159 Covey, C., Gleckler, P. J., Doutriaux, C., Williams, D. N., Dai, A., Fasullo, J., ...  
1160 Berg, A. (2016). Metrics for the diurnal cycle of precipitation: Toward routine  
1161 benchmarks for climate models. *Journal of Climate*, 29(12), 4461 - 4471. doi:  
1162 10.1175/JCLI-D-15-0664.1
- 1163 Danabasoglu, G., Lamarque, J.-F., Bacmeister, J., Bailey, D. A., DuVivier, A. K.,  
1164 Edwards, J., ... Strand, W. G. (2020). The community earth system  
1165 model version 2 (cesm2). *Journal of Advances in Modeling Earth Sys-*  
1166 *tems*, 12(2), e2019MS001916. (e2019MS001916 2019MS001916) doi:  
1167 <https://doi.org/10.1029/2019MS001916>
- 1168 Delworth, T. L., Rosati, A., Anderson, W., Adcroft, A. J., Balaji, V., Benson, R.,  
1169 ... Zhang, R. (2012). Simulated climate and climate change in the gfdl cm2.5  
1170 high-resolution coupled climate model. *Journal of Climate*, 25(8), 2755–2781.  
1171 doi: 10.1175/JCLI-D-11-00316.1
- 1172 Dennis, J., Edwards, J., Evans, K., Guba, O., Lauritzen, P., Mirin, A., ... Worley,  
1173 P. H. (2012). CAM-SE: A scalable spectral element dynamical core for the  
1174 community atmosphere model. *Int. J. High Perf. Comp. Appl.*, 26, 74–89.
- 1175 Dennis, J., Fournier, A., Spatz, W. F., St.-Cyr, A., Taylor, M. A., Thomas, S. J.,  
1176 & Tufo, H. (2005). High resolution mesh convergence properties and parallel  
1177 efficiency of a spectral element atmospheric dynamical core. *Int. J. High Perf.*  
1178 *Comp. Appl.*, 19, 225–235.
- 1179 Dettinger, M. D., Ralph, F. M., Das, T., Neiman, P. J., & Cayan, D. R. (2011). At-  
1180 mospheric Rivers, Floods and the Water Resources of California. *Water*, 3(2),  
1181 445–478. doi: 10.3390/w3020445
- 1182 Doelling, D. R., Loeb, N. G., Keyes, D. F., Nordeen, M. L., Morstad, D., Nguyen,  
1183 C., ... Sun, M. (2013). Geostationary enhanced temporal interpolation for  
1184 ceres flux products. *Journal of Atmospheric and Oceanic Technology*, 30(6),  
1185 1072 - 1090. doi: 10.1175/JTECH-D-12-00136.1
- 1186 Doelling, D. R., Sun, M., Nguyen, L. T., Nordeen, M. L., Haney, C. O., Keyes,  
1187 D. F., & Mlynczak, P. E. (2016). Advances in geostationary-derived longwave  
1188 fluxes for the ceres synoptic (syn1deg) product. *Journal of Atmospheric and*  
1189 *Oceanic Technology*, 33(3), 503 - 521. doi: 10.1175/JTECH-D-15-0147.1
- 1190 Duffy, P. B., Govindasamy, B., Iorio, J. P., Milanovich, J., Sperber, K. R., Taylor,  
1191 K. E., ... Thompson, S. L. (2003). High-resolution simulations of global

- 1192 climate, part 1: present climate. *Clim. Dyn.*, *21*, 371-390.
- 1193 Edman, J. P., & Romps, D. M. (2014). An improved weak-pressure-gradient scheme  
1194 for single-column modeling. *Journal of the Atmospheric Sciences*, *71*(7), 2415–  
1195 2429.
- 1196 Evans, K., Lauritzen, P., Mishra, S., Neale, R., Taylor, M., & Tribbia, J. (2013).  
1197 AMIP simulation with the CAM4 spectral element dynamical core. *J. Climate*,  
1198 *26*(3), 689–709.
- 1199 Field, P. R., Cotton, R. J., McBeath, K., Lock, A. P., Webster, S., & Allan, R. P.  
1200 (2014). Improving a convection-permitting model simulation of a cold air  
1201 outbreak. *Quarterly Journal of the Royal Meteorological Society*, *140*(678),  
1202 124–138.
- 1203 Findeisen, W. (1938). *Kolloid-meteorologische vorgänge bei neiderschlags-bildung*.  
1204 (Vol. 55).
- 1205 Flatau, P. J., Walko, R. L., & Cotton, W. R. (1992). Polynomial fits to saturation  
1206 vapor pressure. *Journal of Applied Meteorology (1988-2005)*, *31*(12),  
1207 1507–1513.
- 1208 Fletcher, J., Mason, S., & Jakob, C. (2016). The Climatology, Meteorology, and  
1209 Boundary Layer Structure of Marine Cold Air Outbreaks in Both Hemispheres.  
1210 *Journal of Climate*, *29*(6), 1999–2014. doi: 10.1175/JCLI-D-15-0268.1
- 1211 Fosser, G., Khodayar Pardo, S., & Berg, P. (2014). Benefit of convection permitting  
1212 climate model simulations in the representation of convective precipitation.  
1213 *Climate Dynamics*, *44*, 45-60. doi: 10.1007/s00382-014-2242-1
- 1214 Gelaro, R., Putman, W. M., Pawson, S., et al. (2015). *Evaluation of the 7-km geos-5*  
1215 *nature run* (Tech. Rep. Series on Glob. Model Data Assim.) Greenbelt MD,  
1216 USA: NASA.
- 1217 Geleyn, J., & Hollingsworth, A. (1979). An economical analytical method for the  
1218 computation of the interaction between scattering and line absorption of radiation.  
1219 *Beitr. Phys. Atmos.*, *52*(1), 1 – 16.
- 1220 Gettelman, A., Liu, X., Ghan, S. J., Morrison, H., Park, S., Conley, A. J., ...  
1221 Li, J.-L. F. (2010). Global simulations of ice nucleation and ice super-  
1222 saturation with an improved cloud scheme in the community atmosphere  
1223 model. *Journal of Geophysical Research: Atmospheres*, *115*(D18). doi:  
1224 <https://doi.org/10.1029/2009JD013797>
- 1225 Gettelman, A., & Morrison, H. (2015). Advanced two-moment bulk microphysics for  
1226 global models. part i: Off-line tests and comparison with other schemes. *Jour-  
1227 nal of Climate*, *28*(3), 1268 - 1287. doi: 10.1175/JCLI-D-14-00102.1
- 1228 Ghan, S. J., & Zaveri, R. A. (2007). Parameterization of optical properties for  
1229 hydrated internally mixed aerosol. *Journal of Geophysical Research: Atmo-  
1230 spheres*, *112*(D10). doi: <https://doi.org/10.1029/2006JD007927>
- 1231 Giorgi, F., & Marinucci, M. R. (1996). A investigation of the sensitivity of  
1232 simulated precipitation to model resolution and its implications for cli-  
1233 mate studies. *Monthly Weather Review*, *124*(1), 148 - 166. doi: 10.1175/  
1234 1520-0493(1996)124<0148:AIOTSO>2.0.CO;2
- 1235 Godoy, W. F., Podhorszki, N., Wang, R., Atkins, C., Eisenhauer, G., Gu, J., ...  
1236 Klasky, S. (2020). Adios 2: The adaptable input output system, a frame-  
1237 work for high-performance data management. *SoftwareX*, *12*, 100561. doi:  
1238 <https://doi.org/10.1016/j.softx.2020.100561>
- 1239 Golaz, J.-C., Caldwell, P. M., Van Roekel, L. P., Petersen, M. R., Tang, Q., Wolfe,  
1240 J. D., ... Zhu, Q. (2019). The DOE E3SM Coupled Model Version 1:  
1241 Overview and Evaluation at Standard Resolution. *Journal of Advances in  
1242 Modeling Earth Systems*, *11*(7), 2089-2129. doi: [https://doi.org/10.1029/  
1243 2018MS001603](https://doi.org/10.1029/2018MS001603)
- 1244 Golaz, J.-C., Larson, V. E., & Cotton, W. R. (2002). A pdf-based model for bound-  
1245 ary layer clouds. part i: Method and model description. *Journal of the Atmo-  
1246 spheric Sciences*, *59*(24), 3540 - 3551. doi: 10.1175/1520-0469(2002)059<3540:

- 1247 APBMFB)2.0.CO;2
- 1248 Grabowski, W. W. (2016). Towards global large eddy simulation: Super-  
1249 parameterization revisited. *Journal of the Meteorological Society of Japan*.  
1250 *Ser. II*, *94*(4), 327-344. doi: 10.2151/jmsj.2016-017
- 1251 Grabowski, W. W., & Smolarkiewicz, P. K. (1999). Crcp: a cloud resolving convec-  
1252 tion parameterization for modeling the tropical convecting atmosphere. *Phys-*  
1253 *ica D: Nonlinear Phenomena*, *133*(1), 171-178. doi: [https://doi.org/10.1016/  
1254 S0167-2789\(99\)00104-9](https://doi.org/10.1016/S0167-2789(99)00104-9)
- 1255 Guan, B., Molotch, N. P., Waliser, D. E., Fetzer, E. J., & Neiman, P. J. (2010).  
1256 Extreme snowfall events linked to atmospheric rivers and surface air temper-  
1257 ature via satellite measurements. *Geophysical Research Letters*, *37*(20). doi:  
1258 10.1029/2010GL044696
- 1259 Guba, O., Taylor, M., & St.-Cyr, A. (2014). Optimization based limiters for the  
1260 spectral element method. *J. Comput. Phys.*, *267*, 176–195. doi: 10.1016/j.jcp  
1261 .2014.02.029
- 1262 Guba, O., Taylor, M. A., Bradley, A. M., Bosler, P. A., & Steyer, A. (2020). A  
1263 framework to evaluate imex schemes for atmospheric models. *Geoscientific*  
1264 *Model Development*, *13*(12), 6467–6480. doi: 10.5194/gmd-13-6467-2020
- 1265 Hannah, W., Bradley, A., Guba, O., Tang, Q., Golaz, J.-C., & Wolfe, J. (2021).  
1266 *Separating physics and dynamics grids for improved computational efficiency in*  
1267 *spectral element earth system models*. (Accepted, *J. Adv. Modeling Earth Sys.*)  
1268 doi: 10.1029/2020MS002419
- 1269 Hartnett, E., & Edwards, J. (2021). The parallelio (pio) c/fortran libraries for scal-  
1270 able hpc performance..
- 1271 Hawcroft, M. K., Shaffrey, L. C., Hodges, K. I., & Dacre, H. F. (2012). How  
1272 much northern hemisphere precipitation is associated with extratropical cy-  
1273 clones? *Geophysical Research Letters*, *39*(24). doi: [https://doi.org/10.1029/  
1274 2012GL053866](https://doi.org/10.1029/2012GL053866)
- 1275 Herrington, A. R., Lauritzen, P. H., Taylor, M. A., Goldhaber, S., Eaton, B. E.,  
1276 Bacmeister, J. T., . . . Ullrich, P. A. (2019). Physics-dynamics coupling with  
1277 element-based high-order galerkin methods: Quasi-equal-area physics grid.  
1278 *Mon. Weath. Rev.*, *147*(1), 69 - 84. doi: 10.1175/MWR-D-18-0136.1
- 1279 Hersbach, H., Bell, B., Berrisford, P., Hirahara, S., Horányi, A., Muñoz-Sabater,  
1280 J., . . . Thépaut, J.-N. (2020). The era5 global reanalysis. *Quarterly*  
1281 *Journal of the Royal Meteorological Society*, *146*(730), 1999-2049. doi:  
1282 <https://doi.org/10.1002/qj.3803>
- 1283 Hewitt, H., Roberts, M., Mathiot, P., Biastoch, A., Blockley, E., Chassignet,  
1284 E., . . . Zhang, Q. (2020). Resolving and parameterising the ocean  
1285 mesoscale in earth system models. *Current Climate Change Reports*. doi:  
1286 10.1007/s40641-020-00164-w
- 1287 Hohenegger, C., Kornbluh, L., Klocke, D., Becker, T., Cioni, G., Engels, J. F., . . .  
1288 Stevens, B. (2020). Climate statistics in global simulations of the atmosphere,  
1289 from 80 to 2.5 km grid spacing. *Journal of the Meteorological Society of Japan*.  
1290 *Ser. II, advpub*. doi: 10.2151/jmsj.2020-005
- 1291 Hou, A. Y., Kakar, R. K., Neeck, S., Azarbarzin, A. A., Kummerow, C. D., Ko-  
1292 jima, M., . . . Iguchi, T. (2014). The global precipitation measurement mis-  
1293 sion. *Bulletin of the American Meteorological Society*, *95*(5), 701 - 722. doi:  
1294 10.1175/BAMS-D-13-00164.1
- 1295 Huffman, G., Stocker, E., Bolvin, D., Nelkin, E., & Tan, J. (2019). *GPM IMERG*  
1296 *Final Precipitation L3 Half Hourly 0.1 degree x 0.1 degree V06*. (Available  
1297 from Goddard Earth Sciences Data and Information Services Center, Accessed  
1298 19 March 2020) doi: 10.5067/GPM/IMERG/3B-HH/06
- 1299 Huffman, G. J., & coauthors. (2019). *Nasa global precipitation measurement (gpm)*  
1300 *integrated multi-satellite retrievals for gpm (imerg)* (NASA Algorithm Theoret-  
1301 ical Basis Doc. No. version 06). Greenbelt MD, USA: NASA.

- 1302 Hunke, E. C., & Lipscomb, W. H. (2008). *CICE: The Los Alamos sea ice model,*  
 1303 *documentation and software, version 4.0* (Tech. Rep. No. LACC-06-012). Los  
 1304 Alamos, NM: Los Alamos National Laboratory.
- 1305 Iorio, J. P., Duffy, P. B., Govindasamy, B., Thompson, S. L., Khairoutdinov, M., &  
 1306 Randall, D. (2004). Effects of model resolution and subgrid-scale physics on  
 1307 the simulation of precipitation in the continental United States. *Clim. Dyn.,*  
 1308 *23*, 243-258.
- 1309 Jian, B., Li, J., Yuxin, Z., He, Y., Wang, J., & Huang, J. (2020, 06). Evaluation  
 1310 of the cmip6 planetary albedo climatology using satellite observations. *Climate*  
 1311 *Dynamics, 54*. doi: 10.1007/s00382-020-05277-4
- 1312 Joan, C., Milbrandt, J., Vaillancourt, P., Chosson, F., & Morrison, H. (2020).  
 1313 Adaptation of the predicted particles properties (p3) microphysics scheme  
 1314 for large-scale numerical weather prediction. *Weather and Forecasting, 35,*  
 1315 2541–2565. doi: 10.1175/WAF-D-20-0111.1
- 1316 Judt, F., Klocke, D., Rios-Berrios, R., Vanniere, B., Ziemer, F., Auger, L., ... Zhou,  
 1317 L. (2021). Tropical Cyclones in Global Storm-Resolving Models. *Journal of the*  
 1318 *Meteorological Society of Japan. Ser. II, adpub.* doi: 10.2151/jmsj.2021-029
- 1319 Jung, T., Gulev, S. K., Rudeva, I., & Soloviov, V. (2006). Sensitivity of extrat-  
 1320 ropical cyclone characteristics to horizontal resolution in the ECMWF model.  
 1321 *Quarterly Journal of the Royal Meteorological Society, 132*(619), 1839–1857.  
 1322 doi: <https://doi.org/10.1256/qj.05.212>
- 1323 Jung, T., Miller, M. J., Palmer, T. N., Towers, P., Wedi, N., Achuthavarier, D.,  
 1324 ... Hodges, K. I. (2012). High-resolution global climate simulations with  
 1325 the ecmwf model in project athena: Experimental design, model climate,  
 1326 and seasonal forecast skill. *Journal of Climate, 25*(9), 3155-3172. doi:  
 1327 10.1175/JCLI-D-11-00265.1
- 1328 Kain, J. S., Weiss, S. J., Bright, D. R., Baldwin, M. E., Levit, J. J., Carbin, G. W.,  
 1329 ... Thomas, K. W. (2008). Some practical considerations regarding horizon-  
 1330 tal resolution in the first generation of operational convection-allowing nwp.  
 1331 *Weather and Forecasting, 23*(5), 931 - 952. doi: 10.1175/WAF2007106.1
- 1332 Kasahara, A. (1974). Various vertical coordinate systems used for numerical weather  
 1333 prediction. *Mon. Weath. Rev., 102*, 509–522.
- 1334 Kato, S., Sun-Mack, S., Miller, W. F., Rose, F. G., Chen, Y., Minnis, P., & Wielicki,  
 1335 B. A. (2010). Relationships among cloud occurrence frequency, overlap,  
 1336 and effective thickness derived from calipso and cloudsat merged cloud verti-  
 1337 cal profiles. *Journal of Geophysical Research: Atmospheres, 115*(D4). doi:  
 1338 <https://doi.org/10.1029/2009JD012277>
- 1339 Kendon, E. J., Roberts, N. M., Senior, C. A., & Roberts, M. J. (2012). Realism  
 1340 of Rainfall in a Very High-Resolution Regional Climate Model. *Journal of Cli-*  
 1341 *mate, 25*(17), 5791–5806. doi: 10.1175/JCLI-D-11-00562.1
- 1342 Khairoutdinov, M., Randall, D., & DeMott, C. (2005). Simulations of the atmo-  
 1343 spheric general circulation using a cloud-resolving model as a superparameteri-  
 1344 zation of physical processes. *Journal of the Atmospheric Sciences, 62*(7), 2136  
 1345 - 2154. doi: 10.1175/JAS3453.1
- 1346 Klein, S. A., McCoy, R. B., Morrison, H., Ackerman, A. S., Avramov, A., Boer,  
 1347 G. d., ... Zhang, G. (2009). Intercomparison of model simulations of mixed-  
 1348 phase clouds observed during the arm mixed-phase arctic cloud experiment.  
 1349 i: single-layer cloud. *Quarterly Journal of the Royal Meteorological Society,*  
 1350 *135*(641), 979-1002. doi: <https://doi.org/10.1002/qj.416>
- 1351 Knapp, K. R., Diamond, H. J., Kossin, J. P., Kruk, M. C., & Schreck, C. J. (2018).  
 1352 International best track archive for climate stewardship (IBTrACS) project,  
 1353 version 4. *NOAA National Centers for Environmental Information.* (Accessed  
 1354 June 2021) doi: <https://doi.org/10.25921/82ty-9e16>
- 1355 Knapp, K. R., Kruk, M. C., Levinson, D. H., Diamond, H. J., & Neumann, C. J.  
 1356 (2010). The international best track archive for climate stewardship (IB-

- 1357 TrACS): Unifying tropical cyclone best track data. *Bulletin of the American*  
 1358 *Meteorological Society*, *91*, 363–376. doi: 10.1175/2009BAMS2755.1
- 1359 Kodama, C., Stevens, B., Mauritsen, T., Seiki, T., & Satoh, M. (2019). A  
 1360 New Perspective for Future Precipitation Change from Intense Extratrop-  
 1361 ical Cyclones. *Geophysical Research Letters*, *46*(21), 12435–12444. doi:  
 1362 <https://doi.org/10.1029/2019GL084001>
- 1363 Krueger, S. K., Morrison, H., & Fridlind, A. M. (2016). Cloud-resolving modeling:  
 1364 Arm and the gcss story. *Meteorological Monographs*, *57*, 25.1 - 25.16. doi: 10  
 1365 .1175/AMSMONOGRAPHS-D-15-0047.1
- 1366 Langhans, W., Schmidli, J., Fuhrer, O., Bieri, S., & Schar, C. (2013). Long-term  
 1367 simulations of thermally driven flows and orographic convection at convection-  
 1368 parameterizing and cloud-resolving resolutions. *Journal of Applied Meteorology*  
 1369 *and Climatology*, *52*(6), 1490 - 1510. doi: 10.1175/JAMC-D-12-0167.1
- 1370 Laprise, R. (1992). The Euler equations of motion with hydrostatic pressure as an  
 1371 independent variable. *Mon. Weath. Rev.*, *120*(1), 197–207.
- 1372 Larson, V. E., & Griffin, B. M. (2013). Analytic upscaling of a local microphysics  
 1373 scheme. part i: Derivation. *Quarterly Journal of the Royal Meteorological Soci-*  
 1374 *ety*, *139*(670), 46–57. doi: <https://doi.org/10.1002/qj.1967>
- 1375 Latham, R., Zingale, M., Thakur, R., Gropp, W., Gallagher, B., Liao, W., ... Li,  
 1376 J. (2003). Parallel netcdf: A high-performance scientific i/o interface. In *Sc*  
 1377 *conference* (p. 39). Los Alamitos, CA, USA: IEEE Computer Society. doi:  
 1378 10.1109/SC.2003.10053
- 1379 Lauritzen, P. H., Bacmeister, J. T., Callaghan, P. F., & Taylor, M. A. (2015).  
 1380 Ncar\_topo (v1.0): Ncar global model topography generation software for un-  
 1381 structured grids. *Geoscientific Model Development*, *8*(12), 3975–3986. doi:  
 1382 10.5194/gmd-8-3975-2015
- 1383 Lauritzen, P. H., Mirin, A. A., Truesdale, J., Raeder, K., Anderson, J. L., Bacmeis-  
 1384 ter, J., & Neale, R. B. (2011, June). Implementation of new diffusion/filtering  
 1385 operators in the CAM-FV dynamical core. *The International Journal of High*  
 1386 *Performance Computing Applications*, *26*(1), 63–73. Retrieved from [https://](https://doi.org/10.1177/1094342011410088)  
 1387 [doi.org/10.1177/1094342011410088](https://doi.org/10.1177/1094342011410088) doi: 10.1177/1094342011410088
- 1388 Lauritzen, P. H., & Williamson, D. L. (2019). A total energy error analysis of dy-  
 1389 namical cores and physics-dynamics coupling in the community atmosphere  
 1390 model (cam). *Journal of Advances in Modeling Earth Systems*, *11*(5), 1309-  
 1391 1328. doi: <https://doi.org/10.1029/2018MS001549>
- 1392 Lavers, D. A., & Villarini, G. (2015). The contribution of atmospheric rivers to pre-  
 1393 cipitation in Europe and the United States. *Journal of Hydrology*, *522*, 382–  
 1394 390. doi: 10.1016/j.jhydrol.2014.12.010
- 1395 Lebassi-Habtezion, B., & Caldwell, P. M. (2015). Aerosol specification in single-  
 1396 column community atmosphere model version 5. *Geoscientific Model Develop-*  
 1397 *ment*, *8*(3), 817–828. doi: 10.5194/gmd-8-817-2015
- 1398 Lee, H.-H., Bogenschutz, P., & Yamaguchi, T. (2021). The Implementation of  
 1399 Framework for Improvement by Vertical Enhancement (FIVE) into Energy  
 1400 Exasacle Earth System Model (E3SM). *Journal of Advances in Modeling Earth*  
 1401 *Systems*, in review.
- 1402 Li, G., & Xie, S.-P. (2014). Tropical biases in cmip5 multimodel ensemble: The ex-  
 1403 cessive equatorial pacific cold tongue and double itcz problems. *Journal of Cli-*  
 1404 *mate*, *27*(4), 1765 - 1780. doi: 10.1175/JCLI-D-13-00337.1
- 1405 Lin, S.-J. (2004). A vertically Lagrangian finite-volume dynamical core for global  
 1406 models. *Mon. Weath. Rev.*, *132*, 2293–2397.
- 1407 Lindborg, E. (1999). Can the atmospheric kinetic energy spectrum be explained by  
 1408 two-dimensional turbulence? *Fluid Mech.*, *388*, 259–288.
- 1409 Liu, X., Ma, P.-L., Wang, H., Tilmes, S., Singh, B., Easter, R. C., ... Rasch,  
 1410 P. J. (2016). Description and evaluation of a new four-mode version of  
 1411 the modal aerosol module (mam4) within version 5.3 of the community at-

- 1412 atmosphere model. *Geoscientific Model Development*, 9(2), 505–522. doi:  
1413 10.5194/gmd-9-505-2016
- 1414 Loeb, N. G., Doelling, D. R., Wang, H., Su, W., Nguyen, C., Corbett, J. G., ...  
1415 Kato, S. (2018). Clouds and the earth’s radiant energy system (ceres) energy  
1416 balanced and filled (ebaf) top-of-atmosphere (toa) edition-4.0 data product.  
1417 *Journal of Climate*, 31(2), 895 - 918. doi: 10.1175/JCLI-D-17-0208.1
- 1418 Love, B. S., Matthews, A. J., & Lister, G. M. S. (2011). The diurnal cycle of pre-  
1419 cipitation over the maritime continent in a high-resolution atmospheric model.  
1420 *Quarterly Journal of the Royal Meteorological Society*, 137(657), 934-947. doi:  
1421 10.1002/qj.809
- 1422 Ma, H.-Y., Chuang, C. C., Klein, S. A., Lo, M.-H., Zhang, Y., Xie, S., ... Phillips,  
1423 T. J. (2015). An improved hindcast approach for evaluation and diagnosis  
1424 of physical processes in global climate models. *J. Adv. Mod. Earth Syst.*, 7,  
1425 1810-1827. doi: <https://doi.org/10.1002/2015MS000490>
- 1426 Madden, R. A., & Julian, P. R. (1971). Detection of a 40–50 day oscillation in the  
1427 zonal wind in the tropical pacific. *Journal of Atmospheric Sciences*, 28(5), 702  
1428 - 708. doi: 10.1175/1520-0469(1971)028<0702:DOADOI>2.0.CO;2
- 1429 Maslowski, W., Clement-Kinney, J., Marble, D., & Jakacki, J. (2008). Towards eddy-  
1430 resolving models of the Arctic Ocean. In M. Hecht & H. Hasumi (Eds.), *Ocean*  
1431 *modeling in an eddying regime* (Vol. 177, pp. 241–264). American Geophysical  
1432 Union.
- 1433 McClean, J. L., Bader, D. C., Bryan, F. O., Maltrud, M. E., Dennis, J. M., Mirin,  
1434 A. A., ... Worley, P. H. (2011). A prototype two-decade fully-coupled  
1435 fine-resolution ccsm simulation. *Ocean Modelling*, 39(1), 10 - 30. (Mod-  
1436 elling and Understanding the Ocean Mesoscale and Submesoscale) doi:  
1437 <https://doi.org/10.1016/j.ocemod.2011.02.011>
- 1438 McClenny, E. E., Ullrich, P. A., & Grotjahn, R. (2020). Sensitivity of atmo-  
1439 spheric river vapor transport and precipitation to uniform sea surface tem-  
1440 perature increases. *Journal of Geophysical Research: Atmospheres*, 125(21),  
1441 e2020JD033421.
- 1442 Milbrandt, J. A., & Morrison, H. (2016). Parameterization of cloud microphysics  
1443 based on the prediction of bulk ice particle properties. part iii: Introduction of  
1444 multiple free categories. *Journal of the Atmospheric Sciences*, 73(3), 975 - 995.  
1445 doi: 10.1175/JAS-D-15-0204.1
- 1446 Mitchell, D. L. (2002). Effective diameter in radiation transfer: General definition,  
1447 applications, and limitations. *Journal of the Atmospheric Sciences*, 59(15),  
1448 2330–2346.
- 1449 Miura, H., Satoh, M., Nasuno, T., Noda, A. T., & Oouchi, K. (2007). A madden-  
1450 julian oscillation event realistically simulated by a global cloud-resolving  
1451 model. *Science*, 318(5857), 1763–1765. doi: 10.1126/science.1148443
- 1452 Miyakawa, T., Satoh, M., Miura, H., Tomita, H., Yashiro, H., Noda, A., ...  
1453 Yoneyama, K. (2014). Madden–julian oscillation prediction skill of a new-  
1454 generation global model demonstrated using a supercomputer. *Nature commu-  
1455 nications*, 5, 3769. doi: 10.1038/ncomms4769
- 1456 Miyamoto, Y., Kajikawa, Y., Yoshida, R., Yamaura, T., Yashiro, H., & Tomita,  
1457 H. (2013). Deep moist atmospheric convection in a subkilometer global  
1458 simulation. *Geophysical Research Letters*, 40(18), 4922-4926. doi:  
1459 <https://doi.org/10.1002/grl.50944>
- 1460 Morrison, H., & Gettelman, A. (2008). A new two-moment bulk stratiform cloud  
1461 microphysics scheme in the community atmosphere model, version 3 (cam3).  
1462 part i: Description and numerical tests. *Journal of Climate*, 21(15), 3642 -  
1463 3659. doi: 10.1175/2008JCLI2105.1
- 1464 Morrison, H., & Grabowski, W. W. (2008). Modeling supersaturation and subgrid-  
1465 scale mixing with two-moment bulk warm microphysics. *Journal of the Atmo-  
1466 spheric Sciences*, 65(3), 792 - 812. doi: 10.1175/2007JAS2374.1

- 1467 Morrison, H., & Milbrandt, J. A. (2015). Parameterization of cloud microphysics  
1468 based on the prediction of the bulk ice particle properties. part i: Scheme  
1469 description and idealized tests. *J. Atmos. Sci.*, *72*, 287–311.
- 1470 Murphy, D. M., & Koop, T. (2005). Review of the vapour pressures of ice and su-  
1471 percooled water for atmospheric applications. *Quarterly Journal of the Royal*  
1472 *Meteorological Society*, *131*(608), 1539–1565. doi: <https://doi.org/10.1256/qj.04>  
1473 .94
- 1474 Na, Y., Fu, Q., & Kodama, C. (2020). Precipitation probability and its future  
1475 changes from a global cloud-resolving model and cmip6 simulations. *Jour-*  
1476 *nal of Geophysical Research: Atmospheres*, *125*(5), e2019JD031926. doi:  
1477 <https://doi.org/10.1029/2019JD031926>
- 1478 Nam, C., Bony, S., Dufresne, J.-L., & Chepfer, H. (2012). The ‘too few, too bright’  
1479 tropical low-cloud problem in cmip5 models. *Geophysical Research Letters*,  
1480 *39*(21). doi: <https://doi.org/10.1029/2012GL053421>
- 1481 Narenpitak, P., Bretherton, C. S., & Khairoutdinov, M. F. (2017). Cloud and circu-  
1482 lation feedbacks in a near-global aquaplanet cloud-resolving model. *Journal of*  
1483 *Advances in Modeling Earth Systems*, *9*(2), 1069–1090. doi: <https://doi.org/10>  
1484 .1002/2016MS000872
- 1485 Nastrom, G., & Gage, K. S. (1985). A climatology of atmospheric wavenumber spec-  
1486 tra of wind and temperature observed by commercial aircraft. *J. Atmos. Sci.*,  
1487 *42*, 950–960.
- 1488 Neale, R. B., Gettelman, A., Park, S., Chen, C.-C., Lauritzen, P. H., Williamson,  
1489 D. L., ... Taylor, M. A. (2012). *Description of the NCAR Community Atmo-*  
1490 *sphere Model (CAM 5.0)* (NCAR Technical Note Nos. TN-486+STR). Boulder  
1491 CO USA: NCAR.
- 1492 Neumann, P., Düben, P., Adamidis, P., Bauer, P., Brueck, M., Kornblueh, L.,  
1493 ... Biercamp, J. (2019). Assessing the scales in numerical weather and  
1494 climate predictions: Will exascale be the rescue? *Philosophical transac-*  
1495 *tions. Series A, Mathematical, physical, and engineering sciences*, *377*. doi:  
1496 [10.1098/rsta.2018.0148](https://doi.org/10.1098/rsta.2018.0148)
- 1497 Noda, A. T., Oouchi, K., Satoh, M., Tomita, H., Iga, S., & Tsushima, Y. (2010).  
1498 Importance of the subgrid-scale turbulent moist process: Cloud distribu-  
1499 tion in global cloud-resolving simulations. *Atmospheric Research*, *96*(2),  
1500 208–217. (15th International Conference on Clouds and Precipitation) doi:  
1501 <https://doi.org/10.1016/j.atmosres.2009.05.007>
- 1502 Ogura, Y. (1963). The evolution of a moist convective element in a shallow, condi-  
1503 tionally unstable atmosphere: A numerical calculation. *Journal of Atmospheric*  
1504 *Sciences*, *20*(5), 407 - 424. doi: [10.1175/1520-0469\(1963\)020<0407:TEOAMC>2](https://doi.org/10.1175/1520-0469(1963)020<0407:TEOAMC>2)  
1505 .0.CO;2
- 1506 Pfahl, S., & Wernli, H. (2012). Quantifying the Relevance of Cyclones for Precipita-  
1507 tion Extremes. *Journal of Climate*, *25*(19), 6770–6780. doi: [10.1175/JCLI-D](https://doi.org/10.1175/JCLI-D)  
1508 -11-00705.1
- 1509 Phillips, T. J., Potter, G. L., Williamson, D. L., Cederwall, R. T., Boyle, J. S., Fior-  
1510 ino, M., ... Yio, J. J. (2004). Evaluating parameterizations in general circula-  
1511 tion models: Climate simulation meet with weather prediction. *Bull. Amer.*  
1512 *Meteor. Soc.*, *85*, 1903–1915. doi: <https://doi.org/10.1175/BAMS-85-12-1903>
- 1513 Pincus, R., Barker, H. W., & Morcrette, J.-J. (2003). A fast, flexible, approx-  
1514 imate technique for computing radiative transfer in inhomogeneous cloud  
1515 fields. *Journal of Geophysical Research: Atmospheres*, *108*(D13). doi:  
1516 <https://doi.org/10.1029/2002JD003322>
- 1517 Pincus, R., Mlawer, E. J., & Delamere, J. S. (2019). Balancing accuracy, efficiency,  
1518 and flexibility in radiation calculations for dynamical models. *Journal of Ad-*  
1519 *vances in Modeling Earth Systems*, *11*(10), 3074–3089. doi: <https://doi.org/10>  
1520 .1029/2019MS001621
- 1521 Pope, V. D., & Stratton, R. A. (2002). The processes governing horizontal resolution

- 1522 sensitivity in a climate model. *Clim. Dyn.*, *19*, 211-236.
- 1523 Prein, A. F., Gobiet, A., Suklitsch, M., Truhetz, H., Awan, N. K., Keuler, K.,  
1524 & Georgievski, G. (2013). Added value of convection permitting sea-  
1525 sonal simulations. *Climate Dynamics*, *41*(9-10), 2655-2677. doi: 10.1007/  
1526 s00382-013-1744-6
- 1527 Prein, A. F., Langhans, W., Fossier, G., Ferrone, A., Ban, N., Goergen, K., ... Le-  
1528 ung, R. (2015). A review on regional convection-permitting climate modeling:  
1529 Demonstrations, prospects, and challenges. *Reviews of Geophysics*, *53*(2),  
1530 323-361. doi: <https://doi.org/10.1002/2014RG000475>
- 1531 Putman, W. M., & Suarez, M. (2011). Cloud-system resolving simulations with  
1532 the nasa goddard earth observing system global atmospheric model (geos-  
1533 5). *Geophysical Research Letters*, *38*(16). doi: [https://doi.org/10.1029/](https://doi.org/10.1029/2011GL048438)  
1534 [2011GL048438](https://doi.org/10.1029/2011GL048438)
- 1535 Randall, D., Khairoutdinov, M., Arakawa, A., & Grabowski, W. (2003). Breaking  
1536 the cloud parameterization deadlock. *Bulletin of the American Meteorological*  
1537 *Society*, *84*(11), 1547 - 1564. doi: 10.1175/BAMS-84-11-1547
- 1538 Rasch, P. J., Xie, S., Ma, P.-L., Lin, W., Wang, H., Tang, Q., ... Shrivastava, M.  
1539 (2019). An overview of the atmospheric component of the Energy Exascale  
1540 Earth System Model. *J. Adv. Model. Earth Sys.*, *11*(8), 2377–2411. doi:  
1541 [10.1029/2019ms001629](https://doi.org/10.1029/2019ms001629)
- 1542 Reynolds, R. W., Rayner, N. A., Smith, T. M., Stokes, D. C., & Wang, W. (2002).  
1543 An improved in situ and satellite sst analysis for climate. *J. Climate*, *15*, 1609-  
1544 1625. doi: [https://doi.org/10.1175/1520-0442\(2002\)015\(1609:AIISAS\)2.0.CO;](https://doi.org/10.1175/1520-0442(2002)015(1609:AIISAS)2.0.CO;2)  
1545 [2](https://doi.org/10.1175/1520-0442(2002)015(1609:AIISAS)2.0.CO;2)
- 1546 Riehl, M., & Malkus, J. (1958). On the heat balance of the equatorial trough. *Geo-*  
1547 *physica (Helsinki)*, *6*, 503-538.
- 1548 Rutz, J. J., Shields, C. A., Lora, J. M., Payne, A. E., Guan, B., Ullrich, P., ... oth-  
1549 ers (2019). The atmospheric river tracking method intercomparison project  
1550 (artmip): quantifying uncertainties in atmospheric river climatology. *Journal*  
1551 *of Geophysical Research: Atmospheres*, *124*(24), 13777–13802.
- 1552 Rémillard, J., & Tselioudis, G. (2015). Cloud Regime Variability over the Azores  
1553 and Its Application to Climate Model Evaluation. *J. Climate*, *28*(24), 9707–  
1554 9720. doi: 10.1175/JCLI-D-15-0066.1
- 1555 Sanders, F., & Gyakum, J. R. (1980). Synoptic-Dynamic Climatology of the  
1556 “Bomb”. *Monthly Weather Review*, *108*(10), 1589–1606. doi: 10.1175/  
1557 [1520-0493\(1980\)108\(1589:SDCOT\)2.0.CO;2](https://doi.org/10.1175/1520-0493(1980)108(1589:SDCOT)2.0.CO;2)
- 1558 Sanderson, B., Piani, C., Ingram, W., Stone, D., & Allen, M. R. (2008). Towards  
1559 constraining climate sensitivity by linear analysis of feedback patterns in thou-  
1560 sands of perturbed-physics gcm simulations. *Clim. Dyn.*, *30*, 175–190. doi:  
1561 [10.1007/s00382-007-0280-7](https://doi.org/10.1007/s00382-007-0280-7)
- 1562 Santos, S. P., Bretherton, C., & Caldwell, P. (2020). Cloud Process Coupling and  
1563 Time Integration in the E3SM Atmosphere Model. *Earth and Space Science*  
1564 *Open Archive*, *34*. (In review at JAMES) doi: 10.1002/essoar.10504538.2
- 1565 Sato, T., Miura, H., Satoh, M., Takayabu, Y. N., & Wang, Y. (2009). Diurnal  
1566 cycle of precipitation in the tropics simulated in a global cloud-resolving  
1567 model. *Journal of Climate*, *22*(18), 4809 - 4826. Retrieved from [https://](https://journals.ametsoc.org/view/journals/clim/22/18/2009jcli2890.1.xml)  
1568 [journals.ametsoc.org/view/journals/clim/22/18/2009jcli2890.1.xml](https://journals.ametsoc.org/view/journals/clim/22/18/2009jcli2890.1.xml)  
1569 doi: 10.1175/2009JCLI2890.1
- 1570 Satoh, M. (2002). Conservative scheme for the compressible nonhydrostatic models  
1571 with the horizontally explicit and vertically implicit time integration scheme.  
1572 *Mon. Weath. Rev.*, *130*, 1227–1245.
- 1573 Satoh, M., Matsuno, T., Tomita, H., Miura, H., Nasuno, T., & Iga, S. (2008). Non-  
1574 hydrostatic icosahedral atmospheric model (nicam) for global cloud resolving  
1575 simulations. *Journal of Computational Physics*, *227*(7), 3486-3514. (Pre-  
1576 dicting weather, climate and extreme events) doi: <https://doi.org/10.1016/>

- 1577 j.jcp.2007.02.006
- 1578 Satoh, M., Stevens, B., Judt, F., Khairoutdinov, M., Lin, S.-J., Putman, W. M., &  
1579 Duben, P. (2019). Global cloud-resolving models. *Curr Clim Change Rep*, *5*,  
1580 172-184. doi: <https://doi.org/10.1007/s40641-019-00131-0>
- 1581 Satoh, M., Tomita, H., Yashiro, H., Miura, H., Kodama, C., Seiki, T., ...  
1582 Kubokawa, H. (2014). The non-hydrostatic icosahedral atmospheric model:  
1583 description and development. *Progress in Earth and Planetary Science*, *1*, 18.  
1584 doi: [10.1186/s40645-014-0018-1](https://doi.org/10.1186/s40645-014-0018-1)
- 1585 Schwartz, C. S., Kain, J. S., Weiss, S. J., Xue, M., Bright, D. R., Kong, F., ...  
1586 Coniglio, M. C. (2009). Next-day convection-allowing wrf model guidance:  
1587 A second look at 2-km versus 4-km grid spacing. *Monthly Weather Review*,  
1588 *137*(10), 3351 - 3372. doi: [10.1175/2009MWR2924.1](https://doi.org/10.1175/2009MWR2924.1)
- 1589 Shapiro, M. A., Fedor, L. S., & Hampel, T. (1987). Research aircraft measure-  
1590 ments of a polar low over the Norwegian Sea. *Tellus A*, *39A*(4), 272-306. doi:  
1591 <https://doi.org/10.1111/j.1600-0870.1987.tb00309.x>
- 1592 Sherwood, S., Bony, S., & Dufresne, J. (2014). Spread in model climate sensitivity  
1593 traced to atmospheric convective mixing. *Nature*, *505*, 37-42. doi: [10.1038/  
1594 nature12829](https://doi.org/10.1038/nature12829)
- 1595 Shi, X., & Liu, X. (2018). Sensitivity study of anthropogenic aerosol indirect forcing  
1596 through cirrus clouds with cam5 using three ice nucleation parameterizations.  
1597 *Journal of Meteorological Research*, *32*(qxxbywb-32-5-shixiangjun), 693. doi:  
1598 [10.1007/s13351-018-8011-z](https://doi.org/10.1007/s13351-018-8011-z)
- 1599 Simmons, A. J., & Burridge, D. M. (1981). An energy and angular momentum con-  
1600 serving vertical finite-difference scheme and hybrid vertical coordinates. *Mon.*  
1601 *Weath. Rev.*, *109*, 758-766.
- 1602 Skamarock, W. C., Klemp, J. B., Dudhia, J., Gill, D. O., Liu, Z., Berner, J., ...  
1603 Huang, X.-Y. (2019). *A Description of the Advanced Research WRF Version 4*  
1604 (Tech. Rep.). Boulder CO, USA: NCAR Tech. Note NCAR/TN-556+STR.
- 1605 Skamarock, W. C., Park, S.-H., Klemp, J. B., & Snyder, C. (2014, October).  
1606 Atmospheric kinetic energy spectra from global high-resolution nonhydro-  
1607 static simulations. *Journal of the Atmospheric Sciences*, *71*(11), 4369-  
1608 4381. Retrieved from <https://doi.org/10.1175/jas-d-14-0114.1> doi:  
1609 [10.1175/jas-d-14-0114.1](https://doi.org/10.1175/jas-d-14-0114.1)
- 1610 Small, R. J., Bacmeister, J., Bailey, D., Baker, A., Bishop, S., Bryan, F., ... Verten-  
1611 stein, M. (2014). A new synoptic scale resolving global climate simulation  
1612 using the Community Earth System Model. *Journal of Advances in Modeling*  
1613 *Earth Systems*, *6*(4), 1065-1094. doi: [10.1002/2014ms000363](https://doi.org/10.1002/2014ms000363)
- 1614 Song, X., & Zhang, G. J. (2011). Microphysics parameterization for convective  
1615 clouds in a global climate model: Description and single-column model  
1616 tests. *Journal of Geophysical Research: Atmospheres*, *116*(D2). doi:  
1617 <https://doi.org/10.1029/2010JD014833>
- 1618 Stephens, G. L., L'Ecuyer, T., Forbes, R., Gettelmen, A., Golaz, J.-C., Bodas-  
1619 Salcedo, A., ... Haynes, J. (2010). Dreary state of precipitation in global  
1620 models. *Journal of Geophysical Research: Atmospheres*, *115*(D24). doi:  
1621 <https://doi.org/10.1029/2010JD014532>
- 1622 Stevens, B., & Bony, S. (2013). What are climate models missing? *Science*,  
1623 *340*(6136), 1053-1054. doi: [10.1126/science.1237554](https://doi.org/10.1126/science.1237554)
- 1624 Stevens, B., Satoh, M., Auger, L., Biercamp, J., Bretherton, C. S., Chen, X., ...  
1625 Zhou, L. (2019). DYAMOND: the DYNAMics of the Atmospheric general circula-  
1626 tion Modeled On Non-hydrostatic Domains. *Progress in Earth and Planetary*  
1627 *Science*, *6*(1), 61. doi: [10.1186/s40645-019-0304-z](https://doi.org/10.1186/s40645-019-0304-z)
- 1628 Steyer, A., Vogl, C. J., Taylor, M., & Guba, O. (2019). Efficient IMEX Runge-Kutta  
1629 methods for nonhydrostatic dynamics. *arXiv e-prints*, arXiv:1906.07219.
- 1630 Storer, R. L., Zhang, G. J., & Song, X. (2015). Effects of convective microphysics  
1631 parameterization on large-scale cloud hydrological cycle and radiative budget

- 1632 in tropical and midlatitude convective regions. *Journal of Climate*, 28(23),  
 1633 9277 - 9297. doi: 10.1175/JCLI-D-15-0064.1
- 1634 Su, H., Jiang, J. H., Teixeira, J., Gettelman, A., Huang, X., Stephens, G., ... Pe-  
 1635 run, V. S. (2011). Comparison of regime-sorted tropical cloud profiles ob-  
 1636 served by cloudsat with geos5 analyses and two general circulation model  
 1637 simulations. *Journal of Geophysical Research: Atmospheres*, 116(D9). doi:  
 1638 https://doi.org/10.1029/2010JD014971
- 1639 Taylor, M. A., & Fournier, A. (2010). A compatible and conservative spectral ele-  
 1640 ment method on unstructured grids. *J. Comput. Phys.*, 229, 5879– 5895. doi:  
 1641 10.1016/j.jcp.2010.04.008
- 1642 Taylor, M. A., Guba, O., Steyer, A., Ullrich, P. A., Hall, D. M., & Eldrid, C. (2020).  
 1643 An energy consistent discretization of the nonhydrostatic equations in prim-  
 1644 itive variables. *Journal of Advances in Modeling Earth Systems*, 12(1). doi:  
 1645 10.1029/2019MS001783
- 1646 Terai, C. R., Caldwell, P. M., Klein, S. A., Tang, Q., & Branstetter, M. L. (2018).  
 1647 The atmospheric hydrologic cycle in the acme v0.3 model. *Climate Dynamics*,  
 1648 50(9), 3251–3279. doi: 10.1007/s00382-017-3803-x
- 1649 Terpstra, A., Michel, C., & Spengler, T. (2016). Forward and Reverse Shear En-  
 1650 vironments during Polar Low Genesis over the Northeast Atlantic. *Monthly*  
 1651 *Weather Review*, 144(4), 1341–1354. doi: 10.1175/MWR-D-15-0314.1
- 1652 Tomita, H., Miura, H., Iga, S., Nasuno, T., & Satoh, M. (2005). A global cloud-  
 1653 resolving simulation: Preliminary results from an aqua planet experiment.  
 1654 *Geophysical Research Letters*, 32(8).
- 1655 Ullrich, P. A., & Zarzycki, C. M. (2017). Tempestextremes: A framework for scale-  
 1656 insensitive pointwise feature tracking on unstructured grids. *Geoscientific*  
 1657 *Model Development*, 10(3), 1069.
- 1658 Viovy, N. (2018). *Crunccep version 7 - atmospheric forcing data for the community*  
 1659 *land model*. Boulder CO: Research Data Archive at the National Center for  
 1660 Atmospheric Research, Computational and Information Systems Laboratory.
- 1661 Wegener, A. (1911). *Thermodynamik der atmosphäre*.
- 1662 Wehner, M. F., Reed, K. A., Li, F., Prabhat, Bacmeister, J., Chen, C.-T., ...  
 1663 Jablonowski, C. (2014). The effect of horizontal resolution on simulation  
 1664 quality in the Community Atmospheric Model, CAM5.1. *Journal of Advances*  
 1665 *in Modeling Earth Systems*, 6(4), 980-997. doi: 10.1002/2013MS000276
- 1666 Weisman, M. L., Skamarock, W. C., & Klemp, J. B. (1997). The resolution de-  
 1667 pendence of explicitly modeled convective systems. *Monthly Weather Review*,  
 1668 125(4), 527 - 548. doi: 10.1175/1520-0493(1997)125<0527:TRDOEM>2.0.CO;2
- 1669 Williamson, D. L., Olson, J. G., Hannay, C., Toniazzo, T., Taylor, M., & Yudin,  
 1670 V. (2015). Energy considerations in the community atmosphere model  
 1671 (cam). *Journal of Advances in Modeling Earth Systems*, 7(3), 1178-1188.  
 1672 doi: https://doi.org/10.1002/2015MS000448
- 1673 Wiscombe, W. J. (1996). *Mie scattering calculations: Advances in technique and*  
 1674 *fast, vector-speed computer codes* (NCAR Technical Note Nos. TN-140+STR).  
 1675 Boulder CO, USA: NCAR.
- 1676 Xie, S., Wang, Y.-C., Lin, W., Ma, H.-Y., Tang, Q., Tang, S., ... Zhang, M. (2019).  
 1677 Improved Diurnal Cycle of Precipitation in E3SM With a Revised Convective  
 1678 Triggering Function. *Journal of Advances in Modeling Earth Systems*, 11(7),  
 1679 2290-2310. doi: https://doi.org/10.1029/2019MS001702
- 1680 Yin, L., Fu, R., Shevliakova, E., & Dickinson, R. (2012). How well can cmip5 sim-  
 1681 ulate precipitation and its controlling processes over tropical south america?  
 1682 *Climate Dynamics*, 41. doi: 10.1007/s00382-012-1582-y
- 1683 Zarzycki, C. M., & Jablonowski, C. (2015). Experimental tropical cyclone forecasts  
 1684 using a variable-resolution global model. *Monthly Weather Review*, 143(10),  
 1685 4012–4037.
- 1686 Zarzycki, C. M., Thatcher, D. R., & Jablonowski, C. (2017). Objective tropical

- 1687 cyclone extratropical transition detection in high-resolution reanalysis and  
 1688 climate model data. *Journal of Advances in Modeling Earth Systems*, 9(1),  
 1689 130–148.
- 1690 Zeng, X., Zhang, Q., Johnson, D., & Tao, W.-K. (2002). Parameterization  
 1691 of wind gustiness for the computation of ocean surface fluxes at differ-  
 1692 ent spatial scales. *Monthly Weather Review*, 130(8), 2125 - 2133. Re-  
 1693 trieved from [https://journals.ametsoc.org/view/journals/mwre/](https://journals.ametsoc.org/view/journals/mwre/130/8/1520-0493_2002_130_2125_powgft_2.0.co_2.xml)  
 1694 [130/8/1520-0493\\_2002\\_130\\_2125\\_powgft\\_2.0.co\\_2.xml](https://journals.ametsoc.org/view/journals/mwre/130/8/1520-0493_2002_130_2125_powgft_2.0.co_2.xml) doi: 10.1175/  
 1695 1520-0493(2002)130(2125:POWGFT)2.0.CO;2
- 1696 Zhang, K., Liu, X., Yoon, J.-H., Wang, M., Comstock, J. M., Barahona, D., &  
 1697 Kooperman, G. (2013). Assessing aerosol indirect effect through ice clouds in  
 1698 cam5. *AIP Conference Proceedings*, 1527(1), 751-751. doi: 10.1063/1.4803379
- 1699 Zhang, S., Fu, H., Wu, L., Li, Y., Wang, H., Zeng, Y., ... Guo, Y. (2020). Opti-  
 1700 mizing high-resolution Community Earth System Model on a Heterogeneous  
 1701 Many-Core Supercomputing Platform (CESM-HR\_SW1.0). *Geoscientific Model*  
 1702 *Development Discussions*, 2020, 1–38. doi: 10.5194/gmd-2020-18
- 1703 Zheng, X., Klein, S., Ghate, V., Santos, S., Mcgibbon, J., Caldwell, P., ... Cadeddu,  
 1704 M. (2020). Assessment of Precipitating Marine Stratocumulus Clouds in  
 1705 the E3SMv1 Atmosphere Model: A Case Study from the ARM MAGIC Field  
 1706 Campaign. *Monthly Weather Review*, 148. doi: 10.1175/MWR-D-19-0349.1
- 1707 Zhu, Y., & Newell, R. E. (1998). A Proposed Algorithm for Moisture Fluxes from  
 1708 Atmospheric Rivers. *Monthly Weather Review*, 126(3), 725–735. doi: 10.1175/  
 1709 1520-0493(1998)126(0725:APAFMF)2.0.CO;2